JOURNAL OF MATERIALS SCIENCE 28 (1993) 700–718

Strength characterization of yttria–partially stabilized zirconia/alumina composite

R. K. GOVILA
Material Systems Reliability Department, Scientific Research Laboratory, MD 2313 Ford Motor Company, PO Box 2053, Dearborn, MI 48121, USA

The flexural strength of yttria–partially stabilized zirconia/alumina composite in the sintered and hot isostatically pressed condition (Super PSZ) was evaluated as a function of temperature (20–1300 °C in air environment), applied stress and time. Failure was essentially governed by the presence of processing defects such as zirconia or alumina agglomerates. The sudden decrease in fracture strength at relatively low temperatures (400–600 °C) is believed to be due to the stability of the tetragonal phase and relative decrease in the extent of the stress-induced martensitic phase transformation of the tetragonal to monoclinic phase. Flexural stress rupture testing at 300–1000 °C in air indicated the material's susceptibility to time-dependent failure, and outlines safe applied stress levels for a given temperature. Stress rupture testing at 1000 °C at low applied stress levels showed bending of specimens, indicating the onset of plasticity or viscous flow of the glassy phase and consequent degradation of material strength.

1. Introduction

During the last 20 years, a variety of high-performance ceramic materials such as silicon nitrides and carbides, sialons, whisker-reinforced ceramic composites and partially-stabilized zirconia (PSZ) have been developed for use as structural components in heat engine applications. Among these ceramics, PSZ is of especial interest due to its high strength and toughness. The use of PSZ materials for insulation and structural components in adiabatic diesel engines [1–4] and other types of industrial applications [5–15] is being investigated. The primary reasons for PSZ use in diesel engine applications are low thermal conductivity (good insulation), high coefficient of thermal expansion (close to cast iron and steel), good oxidation and thermal shock resistance. In general, PSZ usually consists of two or more phases (cubic, tetragonal and monoclinic). The good mechanical properties (bend strength $\geqslant 1000$ MPa and toughness of $\geqslant 10$ MPa m$^{1/2}$ at 20 °C) of PSZ ceramics are primarily a result of stress-induced "martensitic" phase transformation of the metastable tetragonal phase to the stable monoclinic phase, hence the name "transformation toughening". The Y_2O_3 or CeO_2–PSZ can be controlled to contain almost 100% tetragonal zirconia phase [16–19] of sub-micrometre grain size. In spite of the fact that the tetragonal zirconia phase is in the metastable state, these materials are often referred to as "tetragonal zirconia polycrystal" or TZP and have been reviewed by Nettleship and Stevens [20].

Yttria containing tetragonal zirconia (Y–PSZ or Y–TZP) in the sintered state has been studied by several investigators [16–38] and bend strengths of the order of 1000 MPa at room temperature are attainable. Several types of processing, fabrication and material (powder impurity)-related strength-controlling defects [35–38] have been identified in these materials. In general, it appears that in sintered ceramic materials the presence of porosity or porous regions may be the leading cause for degradation of material strength. Furthermore, the porosity or porous regions may or may not be associated with inclusions. Several studies [28, 29, 39, 40] have shown that the bend strength of the sintered Y–PSZ can be significantly increased, in some cases as high as $\geqslant 1500$ MPa by hot isostatic pressing (HIP) [39]. The increased strength is primarily due to reduction or elimination of closed porosity in the sintered material. Similar observations related to increased bend strength were noted earlier by Lange [41–44] in alumina/zirconia composites (better known as zirconia-toughened alumina (ZTA) ceramics) and recently reviewed by Wang and Stevens [45].

Tsukuma *et al.* [46, 47] probably were the first to report that the bending strength of Y–PSZ/Y–TZP can be significantly increased by the addition of sub-micrometre size alumina, followed by sintering and HIPing. This method produced an extremely fine-grained (0.25–0.50 μm size), Y–PSZ/alumina composite consisting of primarily two phases, namely, tetragonal zirconia and α-alumina. Among compositions of alumina varying from 10–40 wt %, the authors [46, 47] found that the highest strength of 2400 MPa (three-point bend) at 20 °C was achieved with 20 wt % alumina addition to Y–PSZ and was independent of the yttria content varying from 2–3 mol %. If these materials are to be used for ceramic components in structural engine applications where temperatures of the order of 200–1000 °C can

0022-2461

easily be attained, it is necessary to characterize the strength behaviour in detail, especially the long-term reliability and durability at temperatures of interest.

This study was undertaken to characterize the strength of a commercially available Y–PSZ/alumina composite both in sintered and HIPed condition by evaluating the fracture strength as a function of temperature (20–1300 °C in air); failure sites and the mode of crack propagation were examined. In addition, long-term reliability and durability behaviour was evaluated using flexural stress rupture testing at several temperatures.

2. Experimental procedure

2.1. Material and fabrication

The multiphase or composite material used in this study was a commercially available tetragonal zirconia polycrystal stabilized with 2.4 mol % yttria and alumina of submicrometre size powder known as "Super-Z" 3Y20A grade obtained from Toyo Soda (now Tosoh) Corporation. The chemical composition of the powder used is shown in Table I as given in the manufacturer's data sheet [48].

TABLE I Typical chemical composition (wt %) for 3Y20A grade powder

ZrO_2	Y_2O_3	Al_2O_3	SiO_2	Fe_2O_3	Na_2O	Ignition loss
75.2	4.2	20	0.01	0.005	0.007	0.6

A total of eight rectangular billets of 5cm × 5cm × 3 cm size were isostatically pressed at room temperature by the wet bag process at 344 MPa. The isopressed billets or blanks were dried at 60 °C for 24 h, then sintered in a Harrop Glo-Bar electric furnace in air at 1454 °C for 2 h and furnace cooled to room temperature. The furnace was heated at 100 °C h^{-1} to 1454 °C. Seven sintered billets were sent out for hot isostatic pressing (HIPing) to IPS, Inc. (London, OH). The billets were HIPed at 1500 °C and 172 MPa in an argon gas environment for 0.5 h.

The bulk density of both sintered and HIPed billets was determined by the water immersion or displacement method. The sintered density varied from 5.465–5.485 g cm^{-3} in eight billets resulting in an average of 5.47 g cm^{-3}. The average density for HIPed billets was 5.51 g cm^{-3}. The tensile surface of flexural specimens in the machined state from sintered and HIPed billets was used for taking X-ray diffraction using CuK_α radiation for 2θ between 24° and 38° [35–37] to determine the presence of tetragonal, monoclinic and cubic zirconia phases. Flexural specimens from sintered and HIPed billets were polished to 1 μm, thermally etched at 1400 °C for 2 h in air, and examined in the SEM in order to reveal the grain size and the microstructure of zirconia and alumina composite matrix.

2.2. Specimen preparation and testing (fast fracture and stress rupture)

Flexural test specimens (approximately 32 mm long × 6 mm wide × 3 mm thick) were machined from both the sintered and HIPed billets. All faces were ground lengthwise using 320 grit diamond wheels; the edges were chamfered (lengthwise) to prevent notch effects. Machined specimens in the finished state from seven sintered and HIPed billets were mixed and randomly picked for testing. All specimens were tested in the as-machined condition and no further surface polishing or any heat treatment was carried out prior to testing. Fracture surfaces of selected specimens were examined in SEM using both secondary electron image (SEI) and back-scattered electron image (BSEI) for surface topography and chemical composition. In addition, elemental distribution or X-ray mapping was done in the SEM with energy dispersive spectroscopy. Complete experimental details of flexural strength evaluation (in a fast fracture mode) at room temperature and above (200–1300 °C), flexural stress rupture testing at elevated temperatures (300 to 1000 °C) in an air environment, self-aligning ceramic test fixture and test span dimensions have been reported previously [49–52].

3. Results and discussion

3.1. Microstructure and phases

X-ray diffraction patterns taken from the sintered, sintered and HIPed (Super PSZ) and Super PSZ annealed at 1038 °C for 24 h in air are shown in Fig. 1a, b and f, respectively. Sintered and Super PSZ composite materials show essentially similar diffraction patterns. The relatively small presence of the monoclinic phase in the sintered and Super PSZ is believed to be due to surface machining of the specimen which transforms the tetragonal phase to monoclinic phase as seen in Fig. 1a and b, and disappears completely upon annealing the specimen at 1038 °C, Fig. 1f, as suggested by Cassidy *et al.* [53].

The microstructure of the Super PSZ is shown in Fig. 2a, and shows a homogeneous distribution of alumina grains in the matrix. The composite matrix primarily consisted of fine-grained tetragonal zirconia of 0.20–0.30 μm size and α-alumina of 0.20–0.50 μm size in an approximately 70/30 vol % ratio as expected from the chemical composition. A higher magnification view of a typical region, boxed area in Fig. 2a, is given in Fig. 2b, and clearly shows the morphology and distribution of zirconia and alumina grains. The dark and white grains marked A and Z were identified as alumina and zirconia, respectively, using energy-dispersive X-ray spectra (Fig. 2), and the matrix appears to be fully dense. The cubic phase zirconia grains are easily identifiable because of their large size (1–10 μm) and cleaved surface morphology [27], and none was seen in the microstructure, Fig. 2b. However, it is important to point out that failure occurring at an agglomerate of large cubic grains was observed in three test specimens (one from the sintered batch and the other two from Super PSZ, Table II) and suggests uneven distribution of yttria in zirconia/alumina composite matrix. It is believed that the

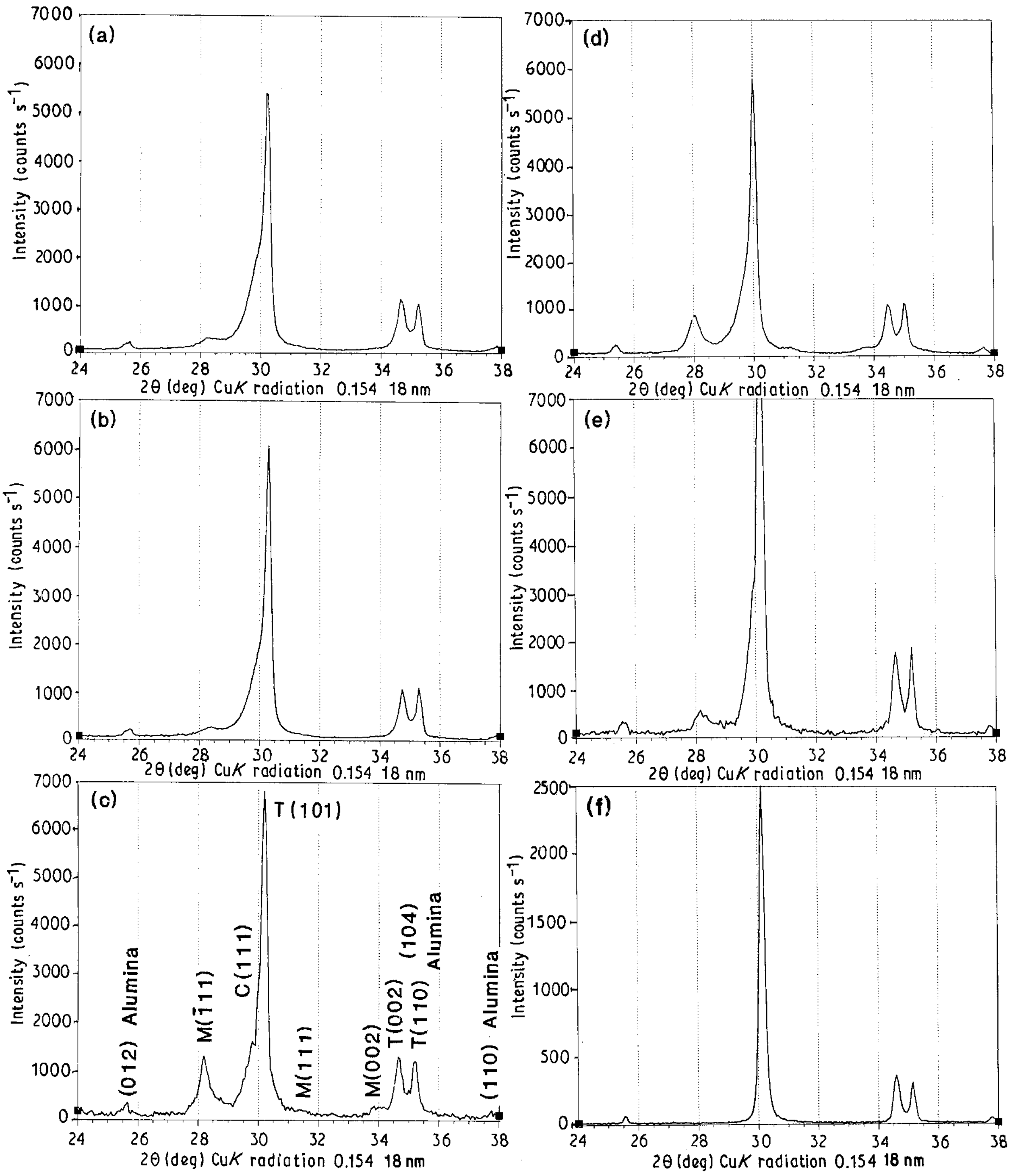

Figure 1 X-ray diffraction patterns of Y–PSZ/alumina composite (3Y20A). The cubic and tetragonal lines overlap and the addition of large amount of alumina to Y–PSZ powder caused slight shifting in cubic (C), monoclinic (M) and tetragonal (T) zirconia lines relative to lines observed in Y–PSZ [17, 35–37]. Note the change in the intensity scale in (f). (a) Sintered Y–PSZ/alumina composite; (b) Super PSZ (sintered + HIPed); (c) Super PSZ, 300 °C, 482 MPa, 529 h, failed; (d) Super PSZ, 300 °C, 482 MPa, 550 h, sustained; (e) Super PSZ, 400 °C, 482 MPa, 30 h, failed; (f) Super PSZ, annealed at 1038 °C for 24 h.

formation of these cubic zirconia grains occurred during sintering.

3.2. Flexural strength versus temperature

3.2.1. Sintered material

The flexural strength was evaluated at 20 °C in order to determine and compare the influence of subsequent HIPing on the microstructure and types of flaws present in this material. A total of ten specimens were tested in four-point bending. A typical statistical variation in fracture strength, σ_F, at 20 °C is shown in Fig. 3. The σ_F varied from a minimum of 816 MPa to a maximum of 1051 MPa with an average strength of 965 MPa, Weibull modulus of 12.7 and a standard deviation of 92 MPa. Examination of the fracture surfaces in all specimens tested at 20 °C showed three types of failure origin, namely, cubic zirconia, agglomerate of fine-grained tetragonal zirconia and porous regions. Among the ten specimens tested, one specimen failed at an agglomerate of large cubic zirconia grains, two specimens failed at fine-grained zirconia agglomerate sites and the majority (the remaining seven) of specimens failed at a porous region, Table II. A typical failure occurring at a subsurface porous region is shown in Fig. 4. Closer examination of the

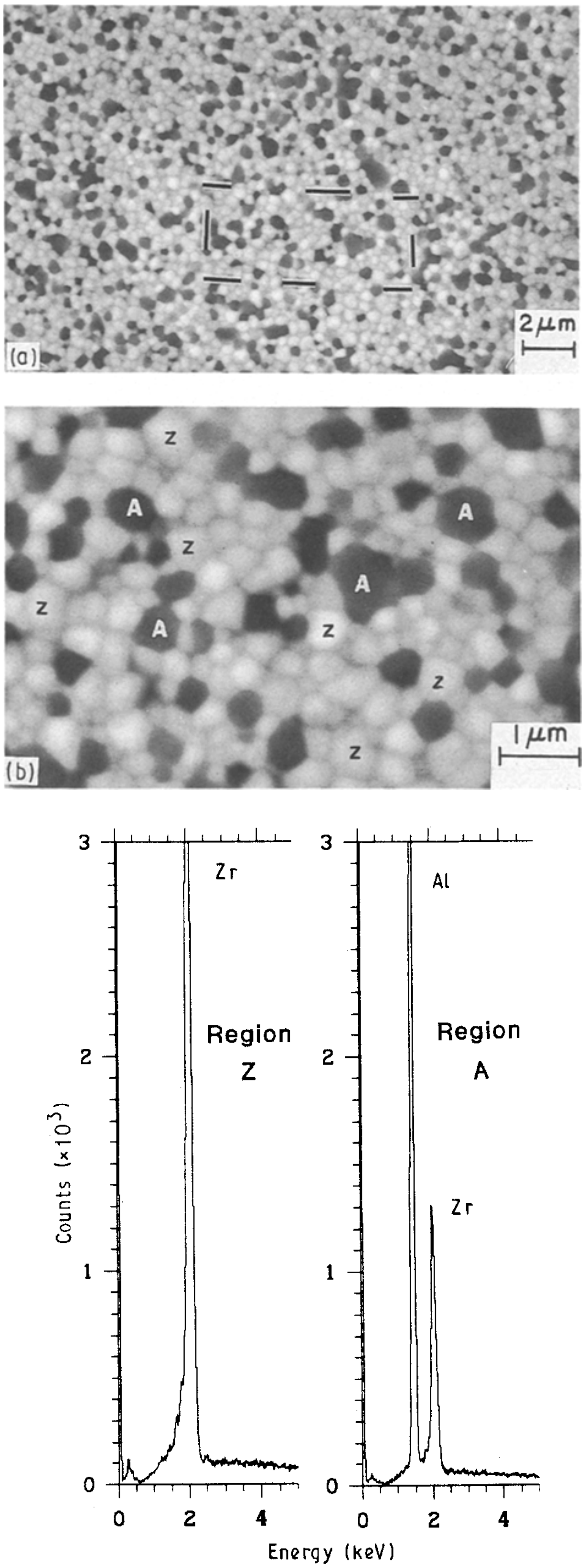

Figure 2 Typical microstructure of Super PSZ as revealed in SEM (SEI) showing uniform distribution of alumina (A) in tetragonal zirconia (Z) matrix.

failure origin revealed the presence of extensive porosity, Fig. 4b. The failure origin appeared like an agglomerate region of either zirconia or alumina grains, but when the same region was examined in BSEI mode for composition, Fig. 4c, it showed normal distribution of zirconia grains, alumina grains and localized regions of porosity (dark-black banded regions).

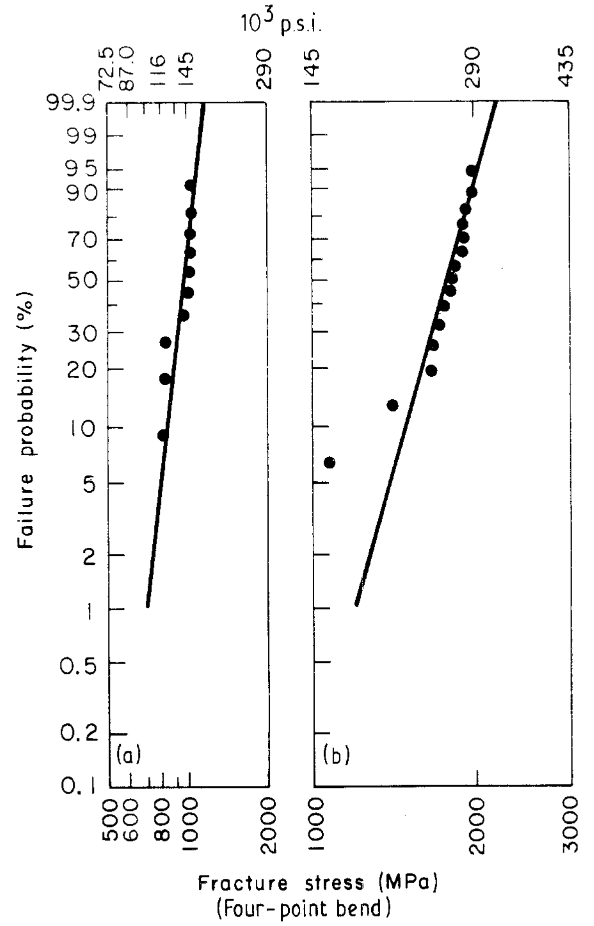

Figure 3 Statistical variation in fracture strength for Y–PSZ/alumina composite (3Y20A) at 20 °C; (a) sintered, (b) sintered and HIPed. (a) $\sigma_{au} \simeq 965$ MPa, S.D. $\simeq 92$ MPa; $m \simeq 12.7$. (b) $\sigma_{au} \simeq 1764$ MPa, S.D. $\simeq 204$ MPa, $m \simeq 10.5$.

In the BSEI mode, the white phase is Y–PSZ/TZP, the light-grey and some black dots are alumina distribution and the dark-black dots are fine porosity in the matrix. Failure-initiating regions varied in size, ranging from 20–100 µm. Examination of the microstructure inside and outside the failure origin (Region 1) revealed distinct differences in grain morphology, Fig. 4d and e, respectively. Inside the failure origin, the grains are rounded and larger in size, Fig. 4d, compared to the grains outside the failure origin or in the matrix, Fig. 4e. This will be discussed further in the case of sintered and HIPed material.

In Y–PSZ/TZP or MgO–PSZ, failure origins are usually associated with porosity and powder impurities such as oxides of silicon, aluminium and iron, and often producing a glassy phase material [32–48, 52]. In this study, none of the failures was associated with powder impurities or inclusions of iron, sodium and silicon or silica.

3.2.2. Sintered and HIPed material (Super PSZ)

This composite material was evaluated in considerable detail because of its unusually high flexural strength (1764 MPa). Hereafter the sintered and HIPed Y–PSZ/alumina (3Y20A) will be referred as Super PSZ.

TABLE II Fast fracture strength data for sintered and HIPed yttria–PSZ/alumina composite

Test no.	Test temp. (°C)	Fracture strength (MPa)	Failure origin, load–deflection (L–D) curve, specimen bending
Sintered material			
1	20	1017	Surface-initiated porous region
2		827	Subsurface porous region
3		971	Surface-initiated cubic zirconia agglomerate
4		838	Subsurface zirconia agglomerate
5		1033	Surface-initiated porous region
6		1018	Surface-initiated porous region
7		1051	Subsurface porous region, Fig. 4
8		1040	Subsurface porous region
9		1042	Subsurface porous region
10		816	Corner failure
Super PSZ (sintered and HIPed material)			
1	20	1922	Unable to identify
2		1726	Unable to identify
3		1408	Unable to identify
4		1994	Unable to identify
5		1922	Subsurface alumina agglomerate
6		1908	Subsurface zirconia agglomerate, Fig. 6
7		1821	Unable to identify
8		1676	Subsurface alumina agglomerate, Fig. 7
9		1765	Unable to identify
10		1654	Subsurface zirconia agglomerate
11		1944	Unable to identify
12		1073	Corner failure, Fig. 5
13		1855	Unable to identify
14		1810	Subsurface zirconia agglomerate
15		1989	Unable to identify
16	200	1624	Unable to identify
17		2030	Unable to identify
18		1651	Unable to identify
19		1722	Subsurface alumina agglomerate
20		1918	Unable to identify
21	400	1222	Surface-initiated failure
22		1187	Surface-initiated failure
23		1307	Subsurface failure
24		1285	Surface-initiated failure
25		1080	Subsurface zirconia agglomerate
26	600	964	Subsurface zirconia agglomerate
27		830	Surface-initiated zirconia agglomerate
28		1258	Subsurface failure
29		901	Surface-initiated zirconia agglomerate
30		637	Subsurface zirconia agglomerate
31		933	Unable to identify
32	800	782	Subsurface failure
33		637	Subsurface zirconia agglomerate
34		849	Surface-initiated failure
35		497	Subsurface zirconia agglomerate, Fig. 9
36		855	Failed at the outer loading edge
37	1000	866	Surface-initiated failure, Fig. 10a
38		581	Failed at the outer loading edge
39		682	Subsurface cubic zirconia agglomerate, Fig. 11
40		487	Failed at the outer loading edge
41		804	Multiple pieces, unable to identify
42	1200	503	Surface-initiated failure, L–D curve linear, no bending
43		335	Subsurface failure, L–D curve linear, no bending, Fig. 13
44		866	Surface-initiated failure, L–D curve shows deviation, no bending, Figs. 12 and 10b
45		441	Subsurface cubic zirconia agglomerate, L–D curve linear, no bending
46		612	Subsurface failure, L–D curve shows deviation, no bending
47	1300	415	Subsurface zirconia agglomerate, L–D curve shows extensive deviation, Fig. 10c, specimen showed bending, Fig. 10d

At room temperature (20 °C), a total of 15 specimens were tested in four-point bending to determine the fast fracture (machine crosshead speed 0.5 mm min^{-1}) strength. A typical statistical variation in fracture strength, σ_F, at 20 °C is shown in Fig. 3. The σ_F varied from a minimum of 1073 MPa to a maximum of 1994 MPa with an average strength of 1764 MPa, Weibull modulus of 10.5, and a stand-

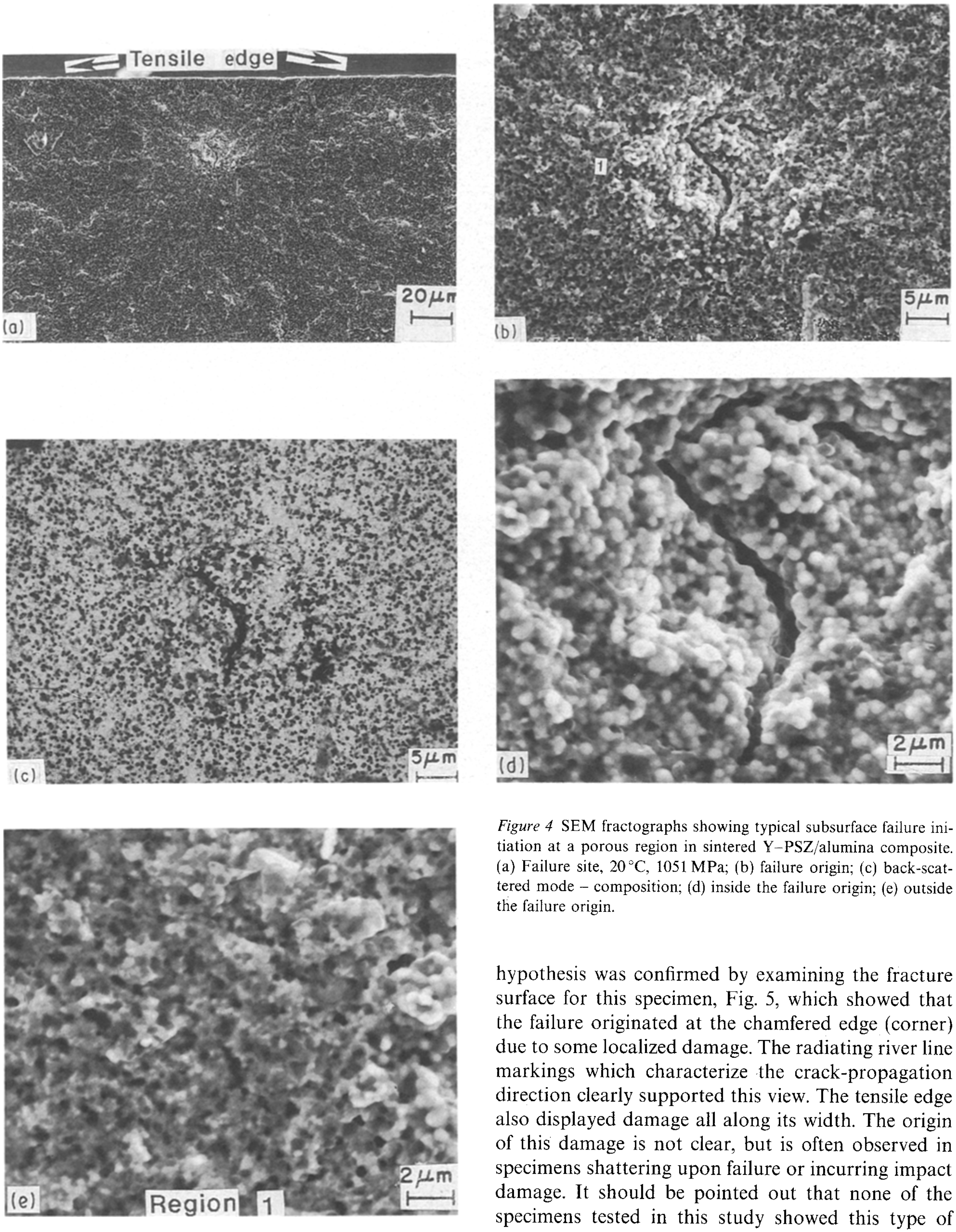

Figure 4 SEM fractographs showing typical subsurface failure initiation at a porous region in sintered Y–PSZ/alumina composite. (a) Failure site, 20 °C, 1051 MPa; (b) failure origin; (c) back-scattered mode – composition; (d) inside the failure origin; (e) outside the failure origin.

ard deviation of 204 MPa. From the statistical distribution, Fig. 3, it is clearly apparent that one of the data points corresponding to the minimum value of 1073 MPa is completely out of alignment with the remaining test data. In the statistical analysis [54], such test data points are referred to as "outlying values" or "outliers" and can simply be identified using the "fourth-spread" method. Using this analysis, the data point corresponding to the 1073 MPa strength is an "outlier" and can be neglected. This hypothesis was confirmed by examining the fracture surface for this specimen, Fig. 5, which showed that the failure originated at the chamfered edge (corner) due to some localized damage. The radiating river line markings which characterize the crack-propagation direction clearly supported this view. The tensile edge also displayed damage all along its width. The origin of this damage is not clear, but is often observed in specimens shattering upon failure or incurring impact damage. It should be pointed out that none of the specimens tested in this study showed this type of damage. The strength data consisting of 14 points showed a minimum of 1408 MPa and a maximum of 1994 MPa with an average strength of 1814 MPa, a Weibull modulus of 14.6 and a standard deviation of 152 MPa. The high value of the Weibull modulus (14.6) obtained from test specimens cut out from several different billets is a strong indication of excellent uniformity in composition, processing and fabrication.

The significantly increased strength of 1814 (or 1764) MPa of Super PSZ relative to 965 MPa for the sintered material is primarily due to the HIPing pro-

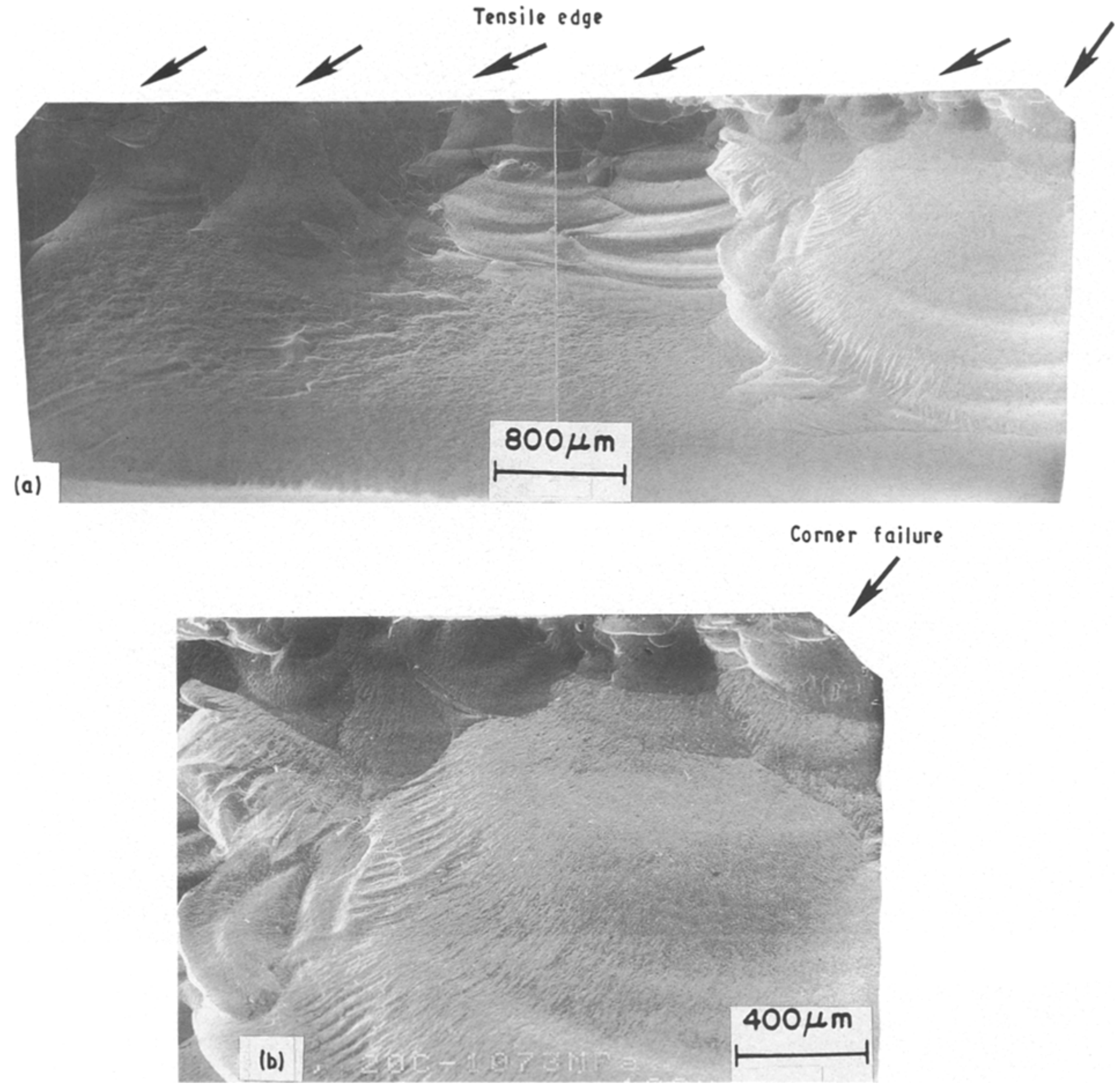

Figure 5 SEM fractographs showing failure initiation at a chamfered edge in a Super PSZ specimen at 20 °C, 1073 MPa.

cess resulting in reduction or elimination of "closed porosity" present in the sintered state. This was confirmed by the absence of any specimen failing at a porous region similar to that seen in the sintered material, Fig. 4. The load–deflection curves for specimens tested at 20 °C displayed non-linear (deviation from the elastic line) behaviour possibly due to stress-induced transformation of the tetragonal phase to monoclinic phase during testing and disappeared at higher temperatures as discussed later. At 20 °C, test specimens shattered upon failure due to the unusually high strength of the material and often broke in more than two pieces. In such cases, failure orgin was difficult to identify. However, in five test specimens, the failure origins were identified, Table II.

Examination of the fracture surfaces revealed only a single type of fracture origin associated with agglomerates. Two types of agglomerate, namely, zirconia and alumina, were observed as failure origins. A typical example of failure occurring at a subsurface site is shown in Fig. 6a. The failure site was examined at a higher magnification and the approximate boundary of the failure origin is shown by the dashed circle, Fig. 6b. Examination by secondary electron image (SEI) in the SEM showed a localized concentration of whitish dots or region, Fig. 6b, at the failure site but failed to reveal the true shape and identity of the failure origin. The same area of the failure region was examined in back-scattered electron image (BSEI) for chemical composition, Fig. 6c. The true shape (elliptical) and size of the failure origin is clearly revealed due to the differences in chemical composition from the surrounding matrix. Similar observations regarding the use of back-scattered electron microscopy or images in revealing failure origins in brittle materials have been reported previously by Healey and Mecholsky [55, 56]. However, the SEI and BSEI modes did not reveal the identity and make-up of the failure origin. The chemical identification of the region inside and outside the failure origin was performed by X-ray mapping the same area at the same magnification as seen in SEI and BSEI modes, Fig. 6b and c,

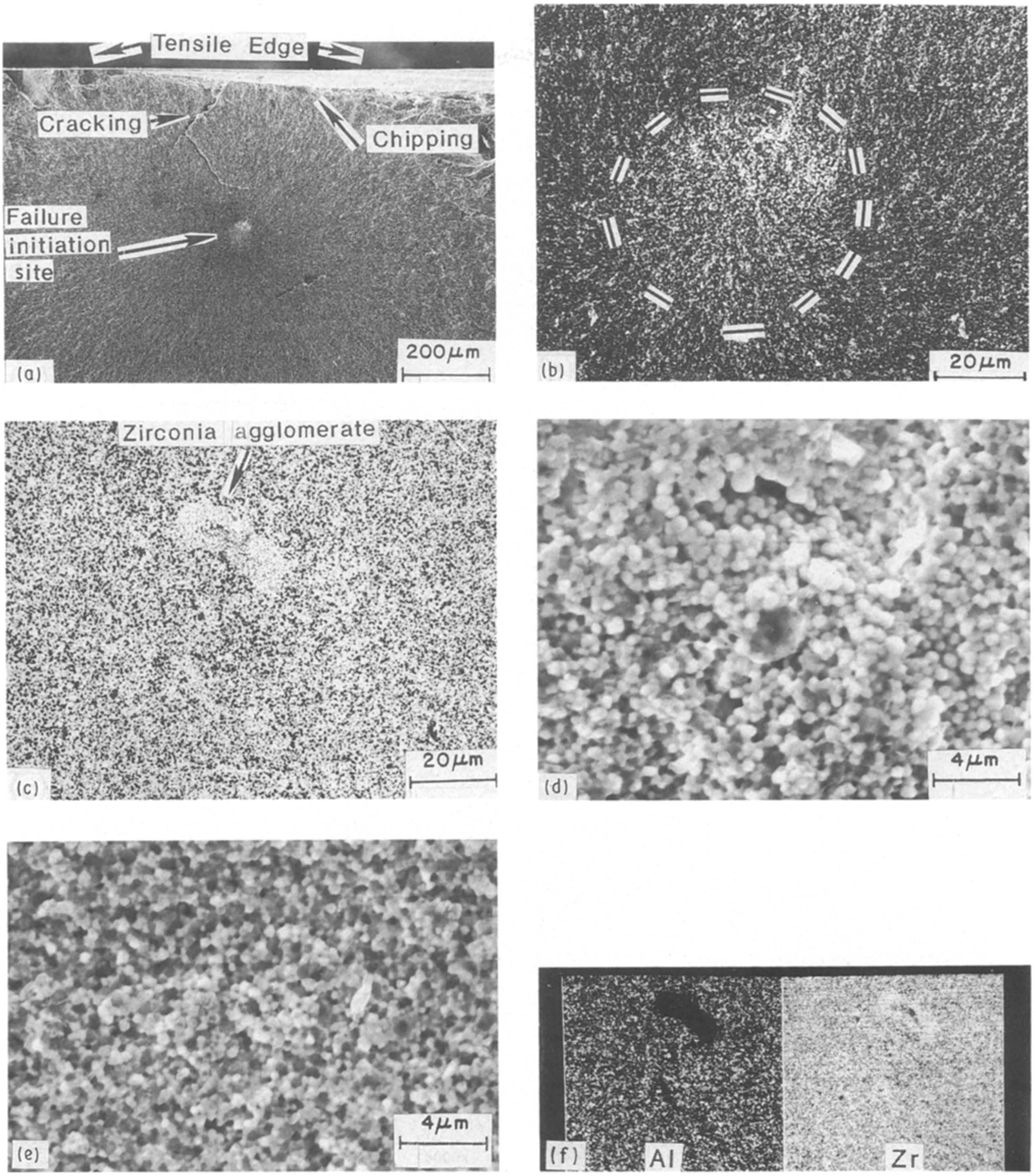

Figure 6 Scanning electron micrographs of subsurface failure initiation in Super PSZ. X-ray maps of failure region taken at the same magnification as seen in (b) but reduced for reproduction. (a) 20 °C, 1908 MPa; (b) failure origin; (c) failure origin, back-scattered mode – composition; (d) inside the failure origin; (e) outside the failure origin; (f) X-ray maps.

respectively. The X-ray maps of the failure region are shown in Fig. 6f, and clearly displayed the shape of the failure origin identical to that seen in BSEI mode, Fig. 6c. In addition, the X-ray maps for elements aluminium and zirconium, Fig. 6f, clearly identified the failure origin as an exclusive zirconia agglomerate. The nature of grains inside the failure origin (centre of the agglomerate region, Fig. 6c) showed the exclusive presence of large tetragonal zirconia grains, and the presence of porosity and cracking, Fig. 6d. The uniformly distributed matrix microstructure showed a slightly finer grain size compared to inside the failure origin as shown in Fig. 6e, and suggests homogeneity in composition, processing (sintering and HIPing) and fabrication (machining).

Another example of failure occurring at a subsurface site is shown in Fig. 7. Examination of the failure site at a higher magnification in SEM using SEI mode showed that the failure origin was approximately of elliptical shape, Fig. 7b. In addition, the failure origin was composed of 12–20 grains, significantly larger than the surrounding matrix grains and darker

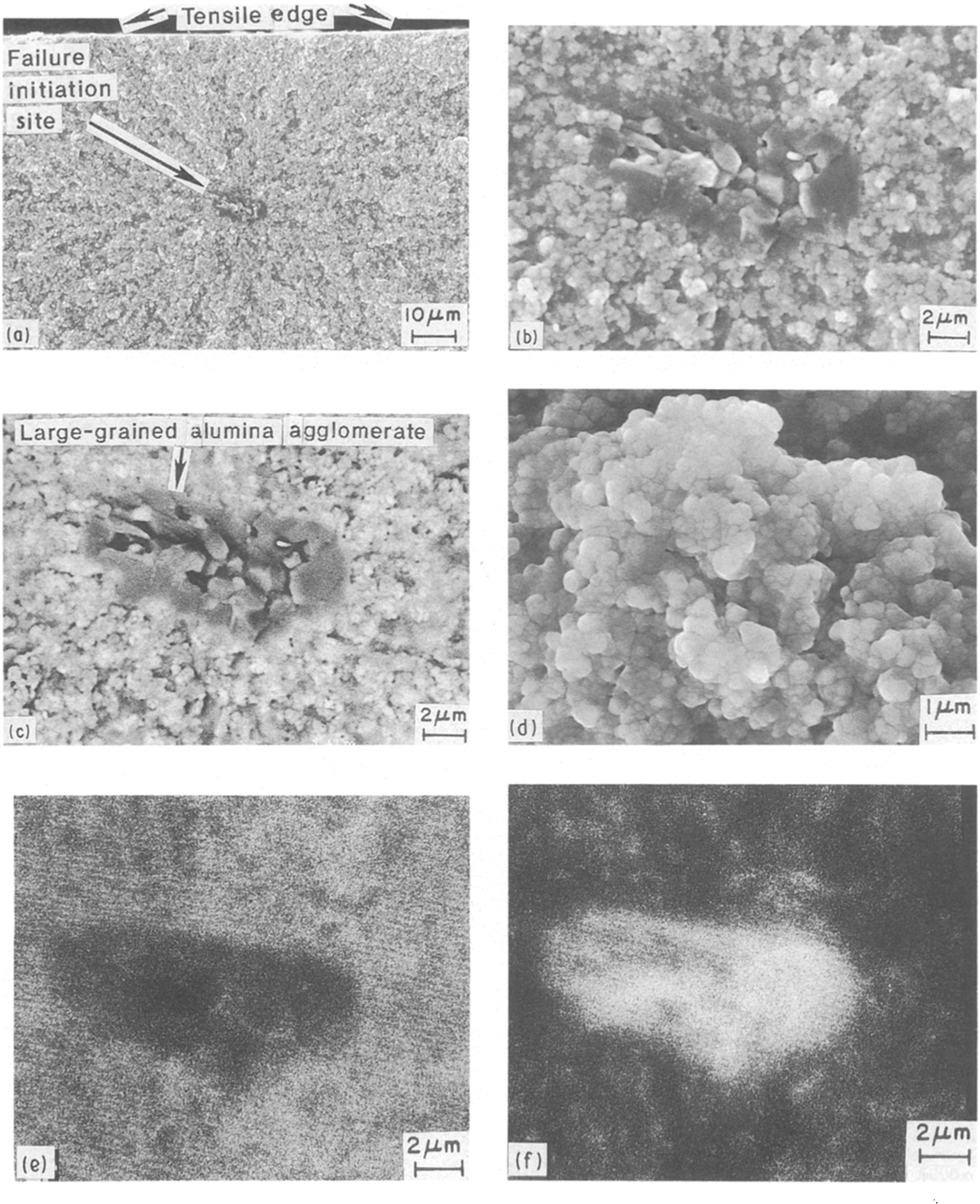

Figure 7 Scanning electron micrographs of subsurface failure initiation in Super PSZ. (a) 20 °C, 1676 MPa; (b) failure origin; (c) failure origin, back-scattered mode – composition; (d) outside the failure origin; (e) X-ray map for zirconium; (f) X-ray map for aluminium.

in shade. At this stage of examination, it is difficult to distinguish whether the darker grains are of alumina or zirconia. However, examination of the same region in BSEI for chemical composition, Fig. 7c, distinctly indicates that the elliptically shaped failure region is made-up of different chemical constituents than the surrounding matrix. X-ray mapping of the failure region for elements zirconium, Fig. 7e, and aluminium, Fig. 7f, revealed that the failure origin was made up of alumina grains. The matrix microstructure showing a uniformly distributed fine grain size is shown in Fig. 7d. From the fractographs (Figs 4–7), it appears that the primary mode of crack propagation during fast fracture (catastrophic failure) was transgranular.

It is important to point out that the room-temperature flexural strength achieved in several billets of Super PSZ is considered to be close to its optimum value, and it is doubtful if the strength can be further improved. This is also reflected by the small size flaws (8–20 μm long) present in the as-fabricated composite. Decreasing the processing related flaw size below 8 μm

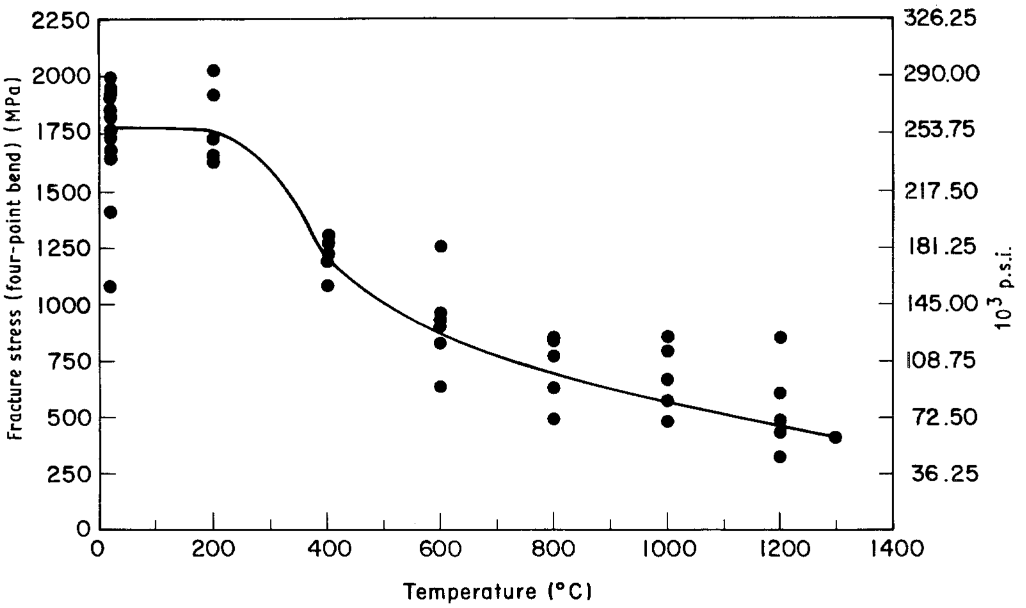

Figure 8 Variation in fast fracture strength of Super PSZ as a function of temperature. All specimens were tested at a machine crosshead speed (MCS) of 0.5 mm min^{-1}. Complete strength data are given in Table II.

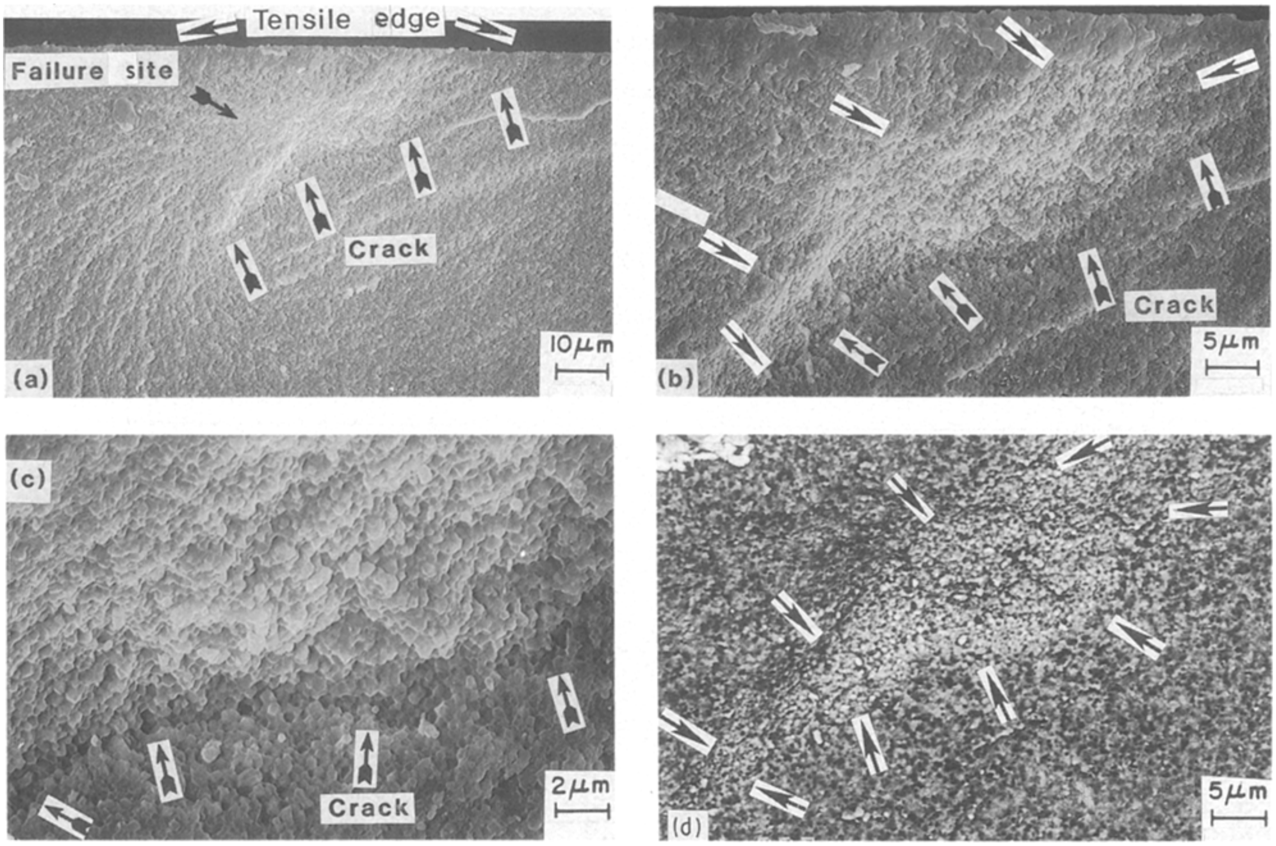

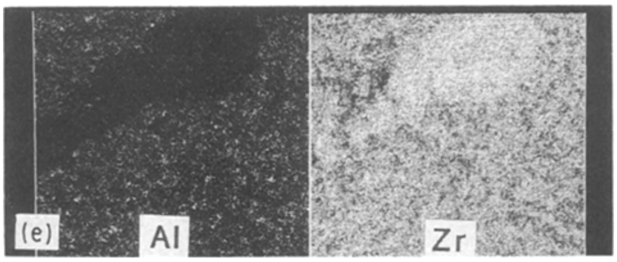

Figure 9 Scanning electron micrographs of failure initiation in Super PSZ. X-ray maps of failure region taken at the same magnification as seen in (b) but reduced for reproduction. (a) 800 °C, 497 MPa; (b) failure origin; (c) inside and outside the failure origin; (d) failure origin, back-scattered mode – composition; (e) X-ray maps.

is an extremely difficult task to achieve especially when the processing parameters involved are clean powder procurement, isopressing, burn-out, sintering and HIPing. The failure-initiating flaws observed in this study were agglomerates of either zirconia or alumina which are primarily processing related, and several studies [37–44, 57–63] have been made of such flaws. Recently, Sung and Nicholson [37] examined in detail the various type of flaws observed in Y–PSZ and showed a reduction in agglomerate formation using either methanol or pH 2 water as a dispersion media for sedimentation of the as-received powder.

Flexural strength was also evaluated at higher temperatures (200–1300 °C) and the variation in σ_F as a function of temperature is shown in Fig. 8. The strength remained essentially constant up to 200 °C and decreased sharply with increasing temperature. The rate of decrease in σ_F is significantly greater in the intermediate temperature range (200–600 °C) compared to higher temperatures (600–1200 °C), Fig. 8. It is believed that the decrease in fracture strength at temperatures as low as 400 and 600 °C is due to an increased stability of the tetragonal phase and decreased extent of the stress-induced martensitic phase transformation of the tetragonal phase to monoclinic phase. This behaviour increases with increasing temperature, hence the decreased fracture strength. The sudden decrease in σ_F from 20 °C (average $\sigma_F = 1764$ MPa) to 600 °C (average $\sigma_F = 961$ MPa) and 800 °C (average $\sigma_F = 724$ MPa) is not encouraging in regard to use of the material at moderately applied stress levels for long-term applications in diesel engine components, as discussed in the next section. Even though all failures originated at the agglomerate region, the size, shape and morphology of the grains varied considerably as illustrated in several examples.

Failure occurring at a subsurface, elongated region in a specimen tested at 800 °C is shown in Fig. 9a. Examination of the failure site at higher magnification is shown in Fig. 9b and the approximate boundary of the failure origin is outlined by the arrows. Examination in BSEI mode, Fig. 9d, revealed that the chemical composition of the failure origin was different from that of the surrounding matrix. This was confirmed by X-ray mapping the same area as viewed in Fig. 9b and d for the presence of elements aluminium

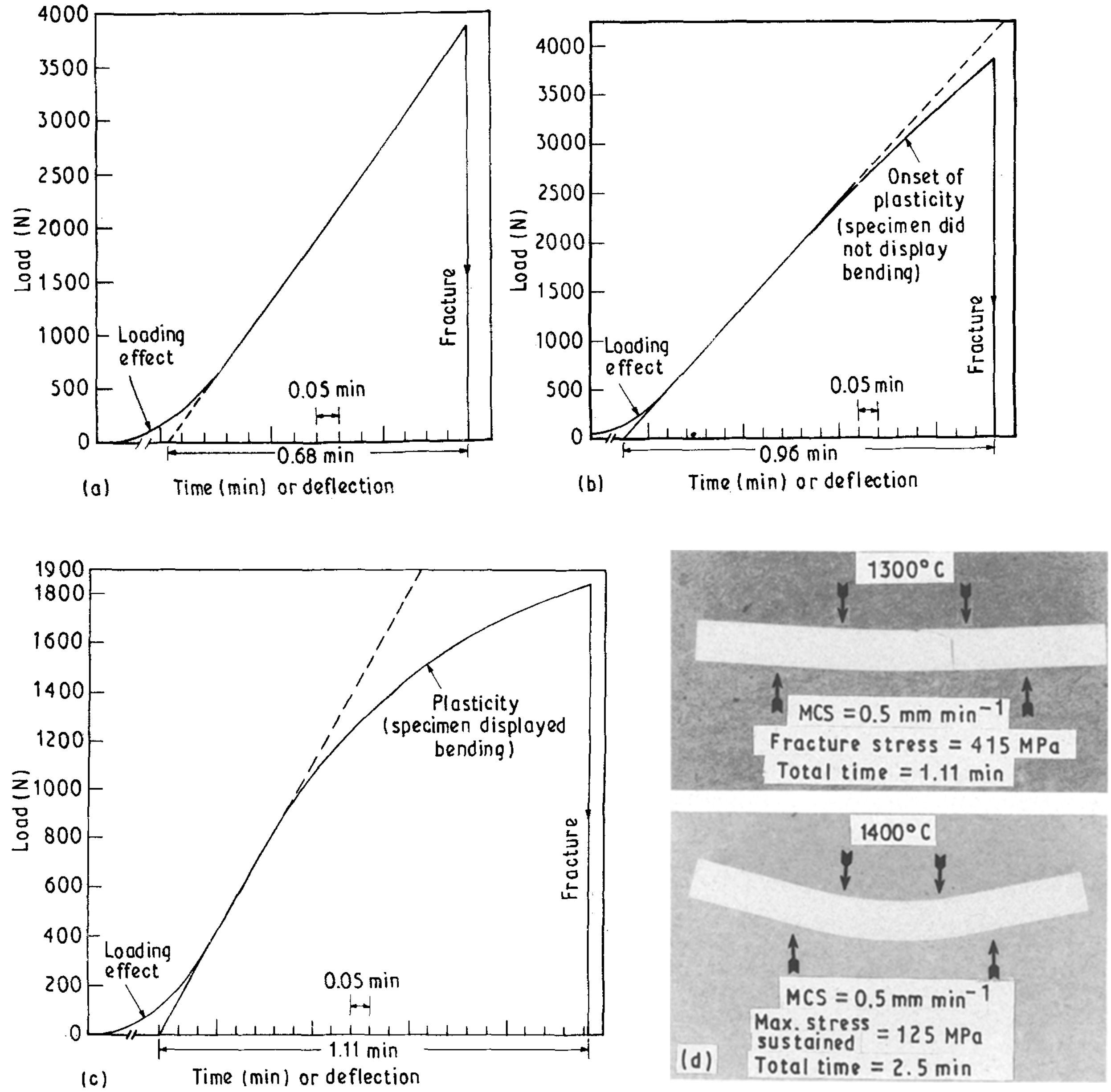

Figure 10 (a–c) Typical traces of load–deflection curves for Super-PSZ specimens tested in four-point bending. (d) Overall view of the flexural specimens of Super PSZ showing bending and fracture at 1300 °C and super plasticity at 1400 °C. Arrows indicate approximate positions of inner and outer loading edges. Machine crosshead speed = 0.5 mm min^{-1}. (a) 1000 °C, fracture strength = 866 MPa; (b) 1200 °C, fracture strength = 866 MPa; (c) 1300 °C, fracture strength = 415 MPa.

and zirconium and revealed that the failure origin was primarily made of an agglomerate of zirconia grains, Fig. 9e. Note the presence of a crack running along the interface of the agglomerate and the matrix, Fig. 9b and c. It is believed that these cracks occurred during the sintering process and were produced either due to mismatch in thermal expansion of the agglomerate (zirconia grains) and the surrounding matrix (zirconia and alumina grains) or the occurrence of phase transformation in the agglomerate upon cooling to room temperature from the higher temperature of sintering. No distinct differences in grain morphology were noticed inside and outside the failure origin, Fig. 9c, in regard to shape and size.

As the testing temperature increased from 800 °C to 1000 °C, the flexural fracture strength showed about the same degree of scatter as that observed at 800 °C, Fig. 8. The load–deflection curves for specimens tested up to 1000 °C in a fast fracture mode (MCS $= 0.5\ \mathrm{mm\,min^{-1}}$) showed completely linear elastic behaviour, Fig. 10a, indicating the absence of creep deformation. However, this is not the case and creep deformation was observed at 1000 °C as discussed in the next section. Failure occurring at a subsurface, large-grained cubic zirconia agglomerate is shown in Fig. 11, and consisted of about 8–10 grains. Failure occurred due to cleavage fracture of the large cubic zirconia grains, Fig. 11b. The failure origin is surrounded by the fine-grained tetragonal zirconia and α-alumina grains, Fig. 11c, showing intergranular crack propagation. The origin and formation of these isolated cubic zirconia agglomerates is not understood and probably happened due to uneven distribution of yttria in Y–PSZ during powder mixing and sintering.

As the test temperature was increased to 1200 °C, considerable scatter in σ_F was noticed due to variations in the type of flaw causing failure, Fig. 8. The first signs of deviation from the elastic behaviour in the load–deflection curve were noticed at 1200 °C suggesting the onset of plasticity or creep deformation, Fig. 10b. The fracture surface for this specimen is shown in Fig. 12. Optical examination of the fracture surface clearly revealed a localized, surface-initiated failure region followed by a mirror region whose boundary is approximately outlined by the dashed lines, Fig. 12a, b. Examination of the failure region showed a plastically deformed semi-circular region of about 12 μm radius, Fig. 12c. The plastically deformed failure-initiating region was examined at a higher magnification in order to reveal the nature of crack propagation inside and outside the failure zone. Inside the failure zone, the matrix grains are separated and the mode of fracture is intergranular, and outside the failure zone, the mode of fracture appears to be a mixed mode consisting of intergranular and transgranular crack propagation, Fig. 12d. It should be pointed out that the failure zone, Fig. 12c, may appear like an agglomerate of zirconia grains (Y–PSZ) but BSEI examination failed to reveal any differences in chemical composition as seen previously in other

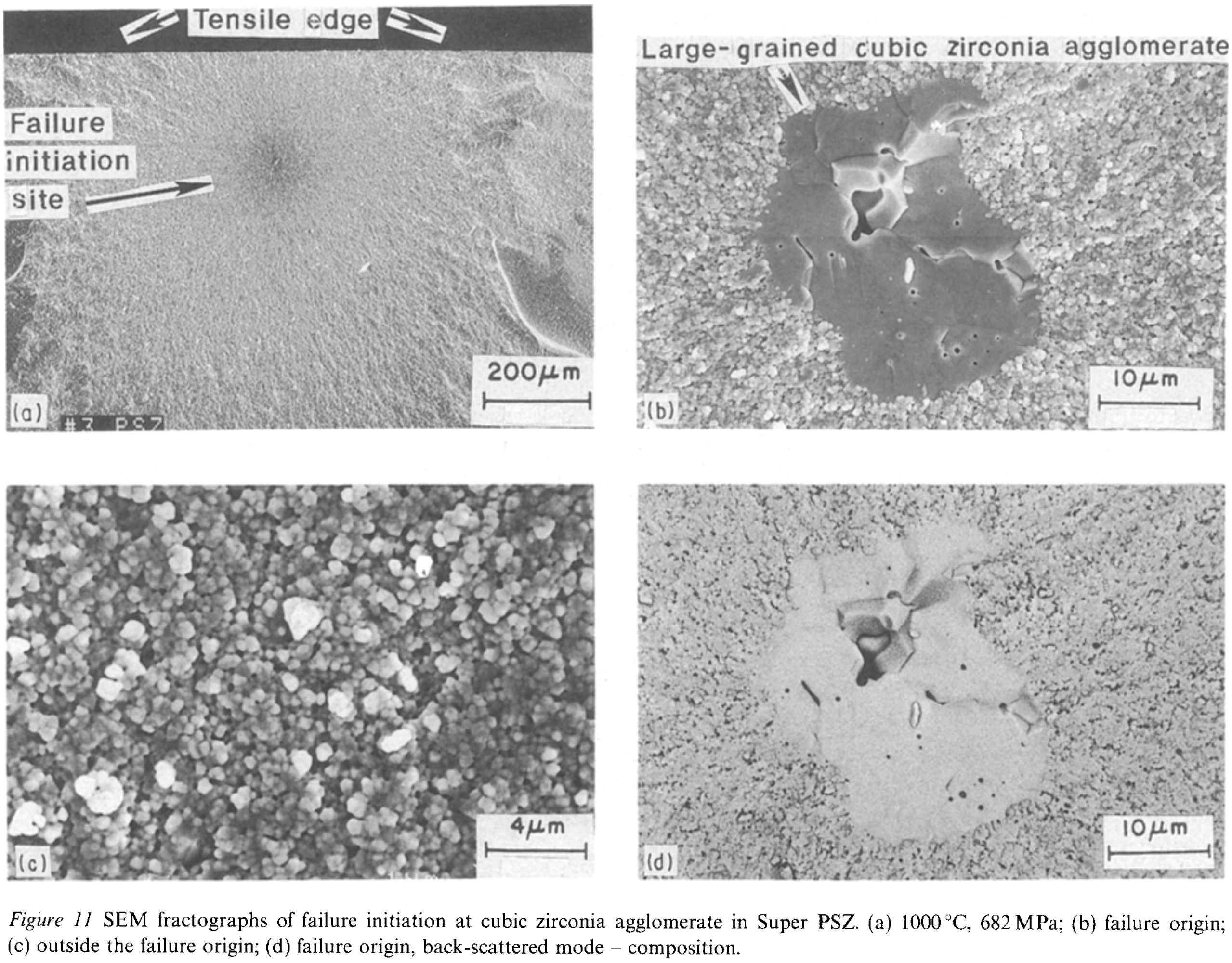

Figure 11 SEM fractographs of failure initiation at cubic zirconia agglomerate in Super PSZ. (a) 1000 °C, 682 MPa; (b) failure origin; (c) outside the failure origin; (d) failure origin, back-scattered mode – composition.

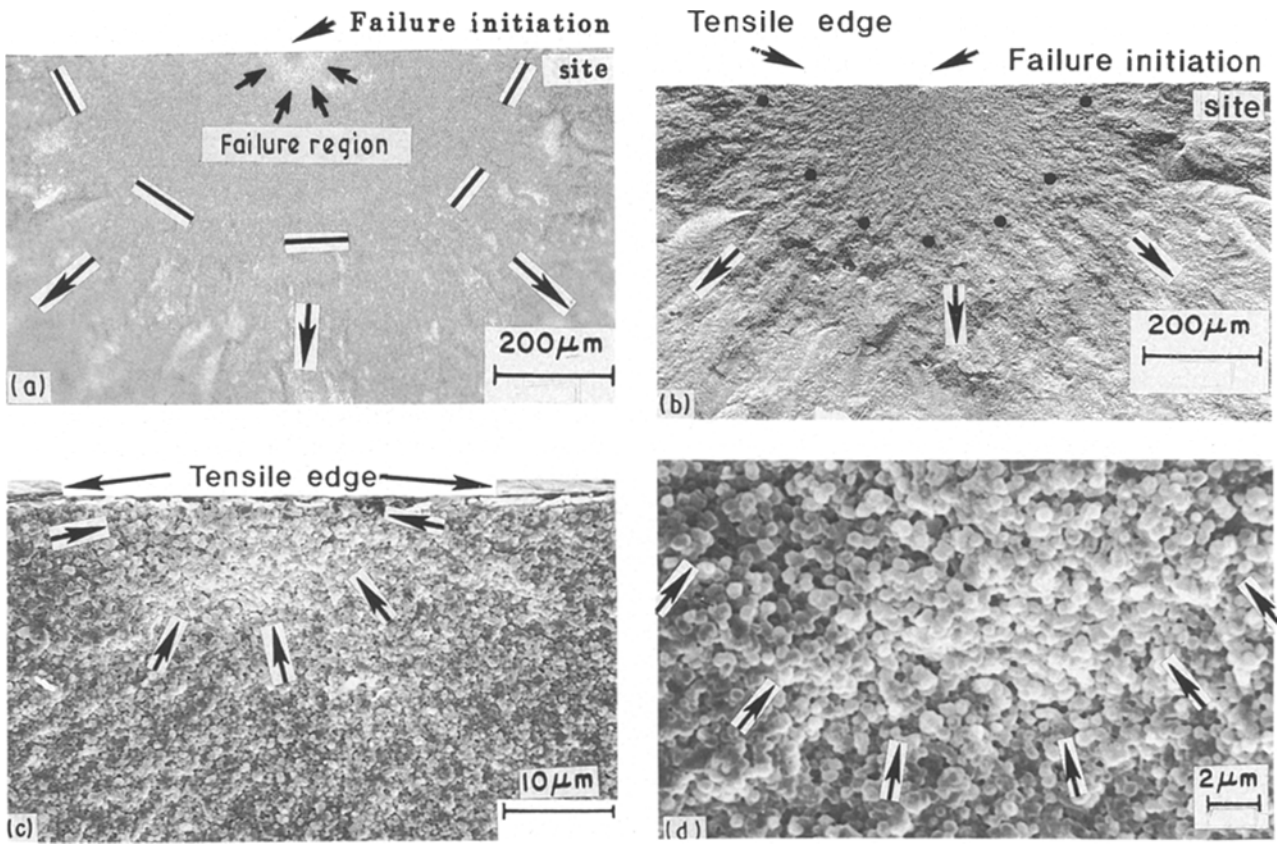

Figure 12 SEM fractographs of surface initiated failure site in Super PSZ. The load–deflection curve for this specimen is shown in Fig. 10b. (a) 1200 °C, 866 MPa; (b) back-scattered electron image – topography; (c) failure zone; (d) inside and outside the failure zone.

specimens. Among the five specimens tested at 1200 °C, only two specimens failing at a higher stress level showed the non-linearity, Table II.

In addition to the onset of plasticity seen at 1200 °C, other samples tested at 1200 °C and failing at relatively low fracture strength levels of 335 and 441 MPa compared to 866 MPa (Fig. 12) displayed the presence of a dark circular region surrounding the failure initiation site as typically shown in Fig. 13a. The load–deflection curve for this specimen showed completely linear behaviour. Examining the failure initiation site at a higher magnification in SEI mode showed cracking or separation along the boundaries of regions 1, 2 and 3, Fig. 13b. When the same area was examined in the BSEI mode, Fig. 13c, it became apparent that the chemical composition of regions 1 and 2 was different relative to the matrix and the approximate sizes were also revealed. It is clear that the failure origin consisted of regions 1 and 2 which were primarily agglomerates of fine-grained zirconia. The interface along the agglomerates and the matrix, Fig. 13d, showed cracking, cavitation and differences in the microstructure. The zirconia grains are rounded and densely packed while the matrix grains (inside the failure zone) are less densely packed and show the presence of grain-boundary separation and cavitation, Fig. 13e. The fine-grained matrix microstructure outside the failure zone consisting of faceted, equiaxed grains is shown in Fig. 13f.

The roundness of zirconia grains in the agglomerate (Fig. 13d, e) suggests the presence of a glassy liquid phase resulting from the presence of silica (SiO_2) as an impurity in the initial powder, Table I. The presence of silica is beneficial in producing improved densification of the ceramic via liquid-phase sintering, but detrimental in degrading the mechanical strength both at 20 °C and higher temperatures due to its presence as a grain-boundary glassy phase, as discussed in detail by Mecartney [64]. Drennan and Hannink [65] have pointed out the benefits of small additions of strontia (SrO) to MgO–zirconia alloys in reducing the deleterious effects of SiO_2. The origin of the dark circular zone surrounding the failure-initiation site and indicated as the "failure zone", Fig. 13a, is not clear and may represent a "slow crack growth region" similar to that observed in sintered and hot-pressed silicon nitrides containing glassy impurities [66, 67].

As the test temperature was increased to 1300 °C, the Super PSZ displayed creep and plastic deformation, Fig. 10c, resulting in decreased fracture strength. Failure was associated with fine-grained zirconia agglomerate region similar to those seen before, and test specimen displayed bending, Fig. 10d. At 1400 °C, test specimens did not fail but continued bending, Fig. 10d, due to "super plastic deformation" of this material as discussed in several studies [68–77].

3.3. Flexural stress rupture

Several studies [78–88] have clearly shown that Y–PSZ or Y–TZP is susceptible to strength degradation during relatively low-temperature (150–400 °C) ageing. The degradation is primarily due to the phase transformation of the tetragonal structure to mono-

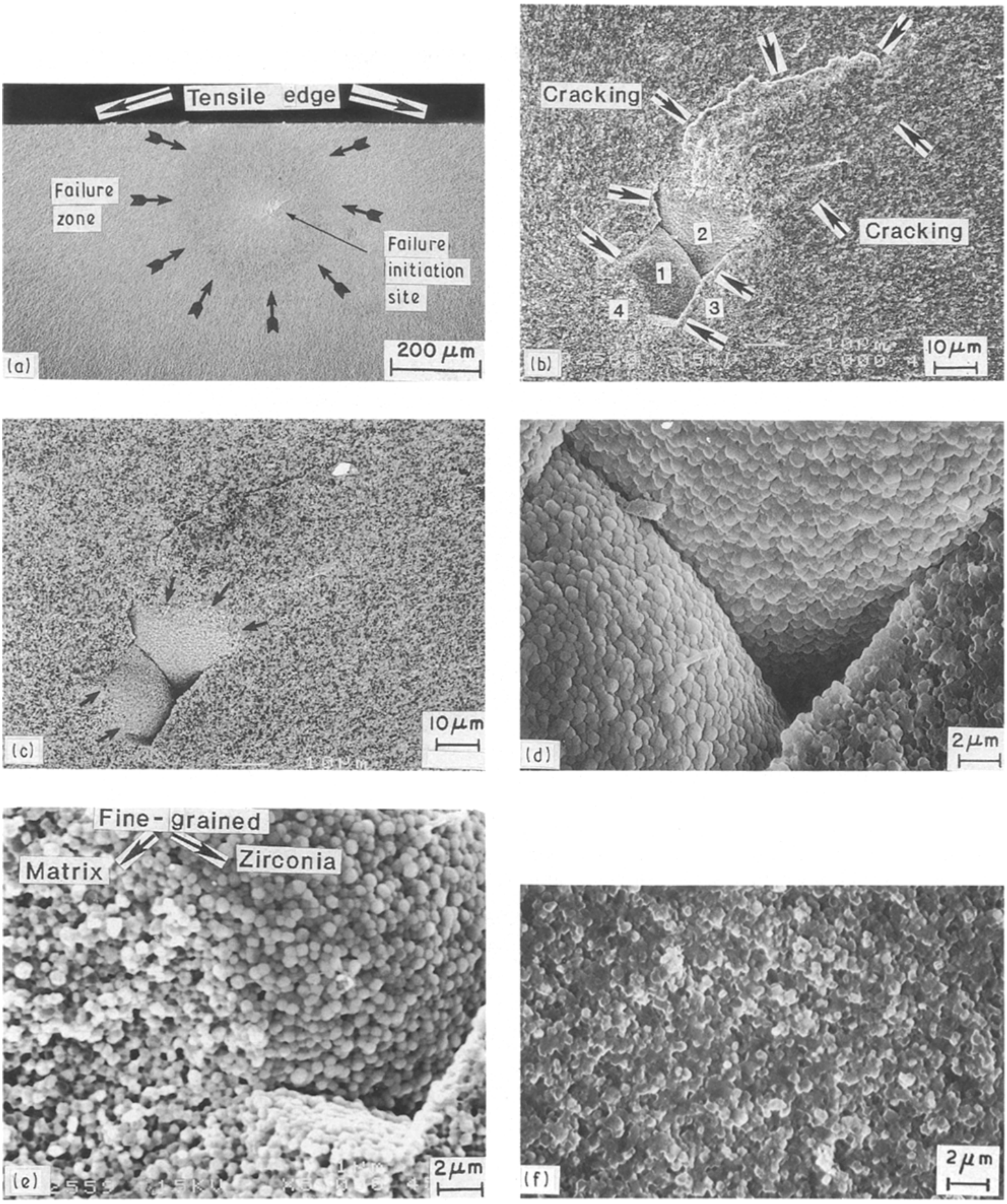

Figure 13 SEM fractographs of failure initiation site in Super PSZ showing changes in grain morphology inside and outside the failure origin. (a) 1200 °C, 335 MPa; (b) failure origin; (c) regions 1 and 2, fine-grained zirconia agglomerate, failure origin, back-scattered mode – composition; (d) failure initiation site, regions 1, 2 and 3; (e) regions 1 and 4, failure origin; (f) fine-grained matrix, outside the failure zone.

clinic, accompanied by micro- and macro-cracking, the severity of which increases between 200 and 300 °C, and the presence of moisture enhances the transformation. The finer grain size (0.20–0.30 μm) of the tetragonal structure and an increase in the yttrium oxide stabilizer content appears to resist the tetragonal to monoclinic transformation, and thereby decreases the tendency for strength degradation. Recently, Cassidy *et al.* [53] have shown that minor modifications in the sintering cycle such as from the usual 24 h at 1450 °C to 1/2–4 h at 1400 or 1450 °C, followed by sintering with a 24 h anneal at 1038 °C, resulted in no degradation in flexural strength of 3YTZP after ageing at 250 °C for long periods (180 days). This proposed sintering and annealing treatment appears to remove all detectable traces of pre-existing monoclinic phase in the Y–PSZ or Y–TZP and prevents further formation during ageing at low temperatures. However, the validity of this proposal has yet to be confirmed. Flexural stress rupture tests

TABLE III Flexural stress rupture results for Super PSZ

Test no.	Test temp. (°C)	Applied stress (MPa)	Failure time (h)	Sustained time without failure (h)	Discoloration, specimen bending and fracture origin
1	20	482	–	4400	None
2	300	482	–	430	Off-white, no bending
3		482	529	–	Off-white, no bending, corner failure, Fig. 14
4		482	–	550	Off-white, no bending,
5	400	482	30	–	Off-white, no bending, zirconia agglomerate, Fig. 15
6		482	36	–	Off-white, no bending, corner failure
7		482	–	503	Off-white, no bending
8	600	482	0	–	Failed instantly, large zirconia sub-surface agglomerate
9		413	–	312	Off-white, no bending, tested in a stepped stress rupture series fashion
		482	–	217	
10		413	–	504	Off-white, no bending, tested in a stepped stress rupture series fashion
		482	–	643	
11		482	–	506	Off-white, no bending
12	800	482	–	530	Off-white, no bending, failed during cooling at the outer loading edge
13		482	–	552	Off-white, no bending
14		482	–	625	Off-white, no bending
15	900	413	–	505	Off-white, no bending, tested in a stepped stress rupture series fashion, failed during cooling at the outer loading edge
		482	–	643	
16	1000	276	–	585	Off-white, showed bending, failed on cooling at the outer loading edge
17		344	0	–	Failed instantly, corner failure, machining damage
18		344	–	72	Off-white, fine bending, Fig. 16
19		413	–	72	Off-white, fine bending, Fig. 16
20		413	–	72	Off-white, fine bending
21		482	0	–	Failed instantly, large zirconia subsurface agglomerate
22		482	–	72	Off-white, bending, Fig. 16
23		482	–	625	Off-white, extensive bending

As-processed material was white in colour.

were carried out as a function of temperature (20–1000 °C) and applied stress in order to determine (a) the material's susceptibility for low-temperature instability, (b) the presence of slow crack growth (SCG), and (c) to identify allowable stress levels for a limited time ($\leqq 500$ h). In all, 23 specimens were tested in the stress rupture mode and the results are summarized in Table III.

At 20 °C, one specimen immersed in water during the entire testing period was tested at an applied stress of 482 MPa and sustained the stress for 6 months (4400 h) without showing failure and bending. The tensile surface of the test specimen was examined by X-ray diffraction to detect the presence of the monoclinic phase. The amount of the monoclinic phase present in this specimen was slightly greater than that seen in the as-machined sample, Fig. 1b, but perhaps not large enough to nucleate microcracks of critical size to cause failure.

At 300 °C, three specimens were tested at an applied stress of 482 MPa. Two specimens sustained the applied stress for over 400 and 500 h without showing failure and bending, and the third specimen failed in 529 h, Table III. The applied stress is relatively low compared to the fast fracture flexural strength of Super PSZ at 300 °C which is over 1000 MPa, Fig. 8. Therefore, this specimen should have survived longer unless either significant formation of the monoclinic phase occurred or some other type of progressive damage (machining, inherent material flaws such as impurities, and process flaws such as agglomerates of zirconia/alumina) formed during the long sustaining stress period and resulting in failure. Examination of the fracture surface showed a smooth tensile edge, Fig. 14a, the failure initiation and subsequent crack propagation appeared to have occurred from the corner, Fig. 14b. No visible and distinguishable "zone of transformation" from the tetragonal to monoclinic phase as seen by Swab [88] was observed in the SEI mode, Fig. 14a, except that in the BSEI mode, a small "disturbed" or "damaged" region whose boundary is marked, Fig. 14c, and indicative of failure initiating site was noticed. No microcracks inside the failure region were visible. An X-ray diffraction pattern taken from the tensile surface* of the fractured specimen is given in Fig. 1c, and clearly shows significant monoclinic phase transformation relative to the as-machined specimen. The fact that another specimen (specimen 4, Table III) tested at the same temperature (300 °C), sustained the stress for 550 h, showed significant amount of monoclinic phase formation, Fig. 1d, and did not fail, suggests that the grains of the monoclinic phase were possibly below a critical size at which failure can be triggered. However, it is difficult

---

* Ideally, the X-ray diffraction pattern should be taken from the fracture face, preferably from the failure initiation region. This would require the use of a "micro-focus X-ray beam camera" to obtain a diffraction pattern and such equipment is not currently used in our laboratory. Also, the cross-sectional area of the fracture surface is relatively small compared to the surface area of the tensile surface of the failed specimen.

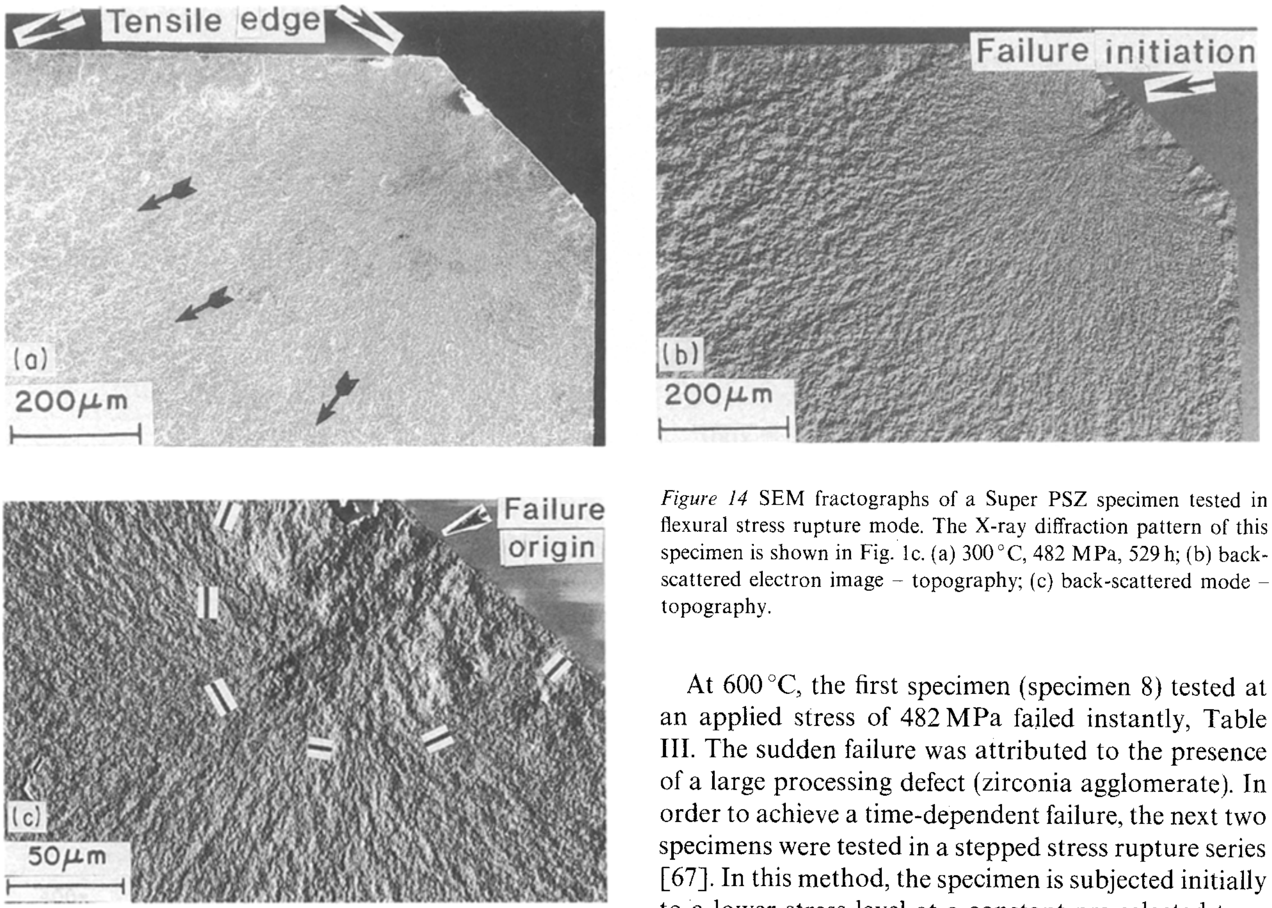

Figure 14 SEM fractographs of a Super PSZ specimen tested in flexural stress rupture mode. The X-ray diffraction pattern of this specimen is shown in Fig. 1c. (a) 300 °C, 482 MPa, 529 h; (b) back-scattered electron image – topography; (c) back-scattered mode – topography.

to determine unequivocally if the failure was a result of the monoclinic phase formation or simply progressive damage occurring around the chamfered edge (corner) under stress over the long duration.

At 400 °C, three specimens were tested at an applied stress of 482 MPa, one sustained the stress for over 500 h without showing bending and failure, one failed in 36 h with failure initiating from the corner similar to that seen at 300 °C (Fig. 14) and one failed in 30 h, Fig. 15. The X-ray diffraction pattern taken from the tensile surface of the fractured specimen, Fig. 15, revealed the formation of the monoclinic phase, Fig. 1e, to a lesser extent than that seen at 300 °C for a specimen subjected to significantly longer duration. Examination of the fracture surface showed that failure initiated at a subsurface, large zirconia agglomerate, Fig. 15, similar to that seen at 800 °C, Fig. 9. The shape and size of the failure origin were identified in BSEI mode, Fig. 15c. The grain morphology inside and outside the failure origin is shown in Fig. 15d–f; a finer grain size is clearly seen outside the failure origin, Fig. 15d and f, a coarser grain size inside the failure origin which progressively increases, attaining a critical size (1 μm) at the centre, Fig. 15e. Clearly, this specimen illustrates that failure at this temperature (or low temperatures, 200–400 °C) is not necessarily due to the presence of the monoclinic phase formation and is primarily due to an inherent processing-related flaw. In short, it is shown that under stress at low temperatures, the formation of the monoclinic phase occurred, but the grains did not achieve a critical size to nucleate microcracks in the matrix and cause failure.

At 600 °C, the first specimen (specimen 8) tested at an applied stress of 482 MPa failed instantly, Table III. The sudden failure was attributed to the presence of a large processing defect (zirconia agglomerate). In order to achieve a time-dependent failure, the next two specimens were tested in a stepped stress rupture series [67]. In this method, the specimen is subjected initially to a lower stress level at a constant pre-selected temperature, and the stress magnitude is increased gradually (after 100–500 h) without interrupting the test. Both specimens sustained the applied stress of 413 and 482 MPa for significantly long periods without showing bending and failure. These observations were confirmed by testing another specimen (specimen 11, Table III) at an applied stress of 482 MPa and sustained the stress for over 500 h without showing bending and failure. Similar behaviour was observed in tests carried out at 800 and 900 °C, Table III.

At 1000 °C, the material showed a distinctly different behaviour to that seen at 800 and 900 °C. A total of eight specimens were tested, two failed prematurely and the remainder sustained the stress without showing failure but displayed bending, indicating the onset of plastic and creep deformation, Table III. At a low applied stress level of 276 MPa, bending of the specimen was visible after 200 h. As the applied stress was increased to 344, 413 and 482 MPa, the extent of bending increased, Fig. 16. It should be noted that these tests point out the importance of stress rupture testing in showing a material's instability (bending) at temperatures of 1000 °C and above, compared to fast fracture testing at similar temperatures which failed to detect the onset of plasticity or creep deformation.

It is important to point out that one specimen at each of these higher temperatures (800, 900, 1000 °C) subjected to 482 MPa and which sustained the stress for over 500 h, failed on cooling at the outer loading edge marks, Table III. In these cases, the furnace door was opened to room temperature after terminating the test and possibly led to cracking at the loading edge. In all three specimens, fracture surfaces showed an identical pattern of microcrack initiation from the

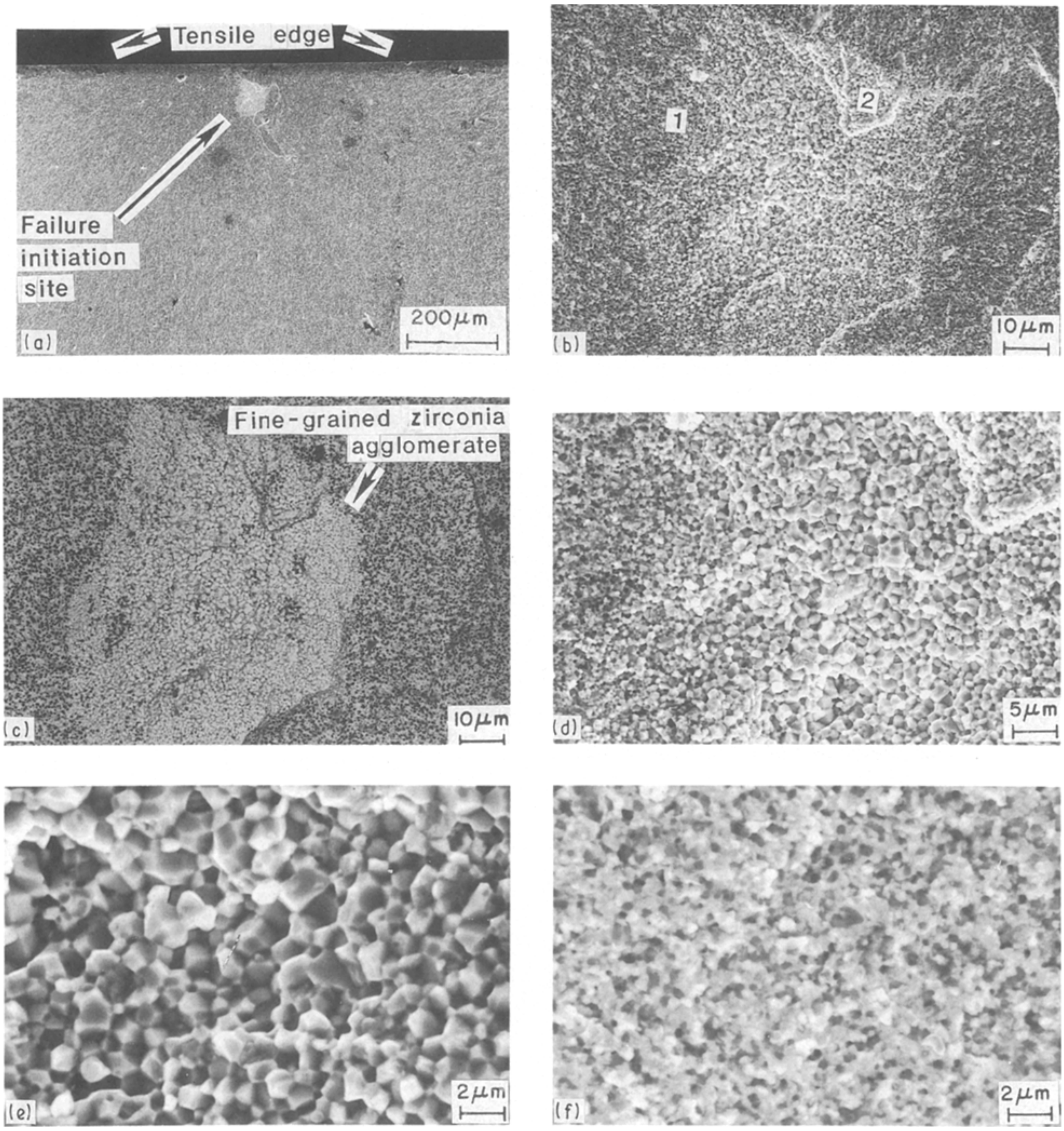

Figure 15 SEM fractographs of a Super PSZ specimen tested in flexural stress rupture mode. The X-ray diffraction pattern of this specimen is shown in Fig. 1e. (a) 400 °C, 482 MPa, 30 h; (b) failure origin; (c) failure origin, back-scattered mode – composition; (d) failure origin, regions 1 and 2; (e) failure origin, centre region; (f) outside the failure origin.

tensile edge. The sudden failure on cooling strongly suggests that the Super PSZ was susceptible to thermal shock. Recently, Lutz *et al.* [89, 90] have investigated the *R*-curve and thermal shock behaviour of Duplex ceramics (large spherical pressure zones of a component B which are fractions of monoclinic zirconia particles dispersed homogeneously in a ceramic matrix of composition A (Y–PSZ/Y–TZP–alumina composite)) including a composite material similar to Super PSZ. They found that 3YZ20A, both in the sintered and sintered and HIPed condition, showed a flat *R*-curve behaviour and also suffered extremely severe strength degradation upon thermal shocking above $\Delta T_C > 200\,^\circ\mathrm{C}$ (critical quenching temperature difference).

4. Conclusion

The yttria-containing tetragonal zirconia/alumina composite (3Y20A) can be fabricated in large batches of fine-grained (0.25–0.30 μm) microstructure with a homogeneous distribution of alumina grains in the matrix. In the sintered condition, failure of specimens was primarily governed by the porosity.

HIPing of the sintered composite eliminated or reduced the closed porosity and thereby increased the flexural strength significantly. Super PSZ appeared to have optimum flexural strength, and strength-controlling flaws as small as 8–10 μm long were observed. Failure was primarily governed by the presence of processing defects like an agglomerate of zirconia or alumina. Zirconia agglomerates dominated the failure.

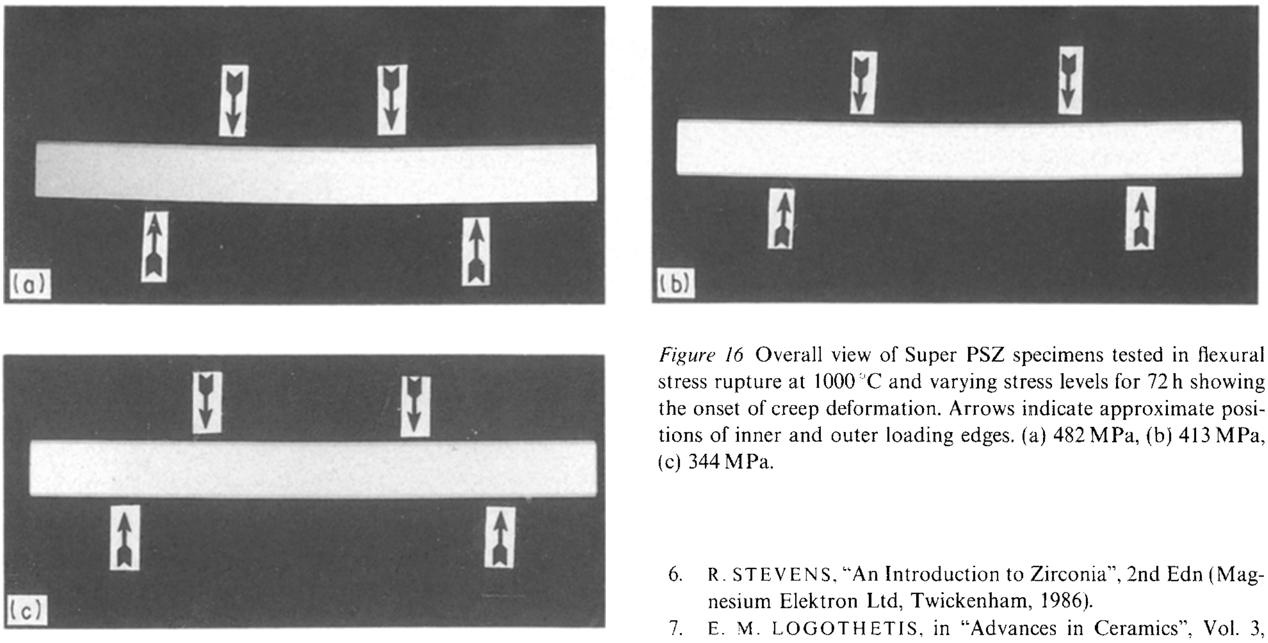

Figure 16 Overall view of Super PSZ specimens tested in flexural stress rupture at 1000 °C and varying stress levels for 72 h showing the onset of creep deformation. Arrows indicate approximate positions of inner and outer loading edges. (a) 482 MPa, (b) 413 MPa, (c) 344 MPa.

The shape and size of failure-causing defects were revealed using BSEI methods.

Flexural strength decreased significantly with increasing temperature and this effect was noticeable at temperatures as low as 400 and 600 °C. Failure occurred in a brittle manner, the mode of crack propagation during fast fracture was primarily transgranular up to 800 °C, and above 800 °C was a mixture of transgranular and intergranular crack growth.

Extensive flexural stress rupture evaluation in the temperature range 300–1000 °C has identified the stress levels for time-dependent and time-independent failures. In addition, stress rupture testing at 1000 °C clearly revealed the onset of plastic deformation or viscous flow of the glassy phase leading to grain-boundary sliding (creep deformation) and consequent degradation of material strength.

Acknowledgements

The author thanks colleague D. Cassidy for making and providing the composite material for evaluation, several colleagues, especially, C. Peters for X-ray diffraction, Y. T. Lu and Dr W. T. Donlon for SEM work, without whom the work would not have been possible to carry out.

References

1. W. BRYZIK and R. KAMO, "Tacom/Cumins Adiabatic Engine Program", 1983 International Congress and Exposition, SAE Paper 830314, Detroit, MI, February 1983.
2. M. MARMACH, D. SERVENT, R. H. J. HANNINK, M. J. MURRAY and M. V. SWAIN, "Toughened PSZ Ceramics – Their Role as Advanced Engine Components", *ibid.*, paper 830318.
3. M. E. WOODS, W. F. MANDLER Jr and T. L. SCOFIELD, *Ceram. Bull.* **64** (1985) 287.
4. D. W. RICHERSON, *ibid.* **64** (1985) 282.
5. R. H. J. HANNINK, M. MARMACH, M. J. MURRAY and M. V. SWAIN, in "Proceedings of the Eleventh Australian Ceramic Conference", Sydney, Australia (Australian Ceramic Society, 1984) p. 57.
6. R. STEVENS, "An Introduction to Zirconia", 2nd Edn (Magnesium Elektron Ltd, Twickenham, 1986).
7. E. M. LOGOTHETIS, in "Advances in Ceramics", Vol. 3, "Science and Technology of Zirconia", edited by A. H. Heuer and L. W. Hobbs (American Ceramic Society, Columbus, OH, 1981) p. 388.
8. R. C. GARVIE, C. URBANI, D. R. KENNEDY and J. C. McNEUER, *J. Mater. Sci.* **19** (1984) 3224.
9. R. C. GARVIE, in "Advances in Ceramics", Vol. 12, Science and Technology of Zirconia, edited by N. Claussen, M. Ruhleand, A. H. Heuer (American Ceramic Society, Columbus, OH, 1984) pp. 465–79.
10. U. DWORAK, H. OLAPINSKI, D. FINGERLE and U. KROHN, *ibid.*, pp. 480–87.
11. P. BOCH, P. FAUCHAIS, D. LOMBARD, B. ROGEAUX and M. VARDELLE, *ibid.*, pp. 488–502.
12. D. S. SUHR, T. E. MITCHELL and R. J. KELLER, *ibid.*, pp. 503–17.
13. F. J. ESPER, K. H. FRIESE and A. H. GEIER, *ibid.*, pp. 528–36.
14. R. V. ALLEN, W. E. BORBIDGE and P. T. WHELAN, *ibid.*, pp. 537–43.
15. Y. Y. WU and S. T. ZHAO, in "Third International Symposium on Ceramic Materials and Components for Engines", Las Vegas, NV, 27–30 November 1988, edited by V. J. Tennery (The American Ceramic Society, Westerville, 1989) p. 1202.
16. P. H. RIETH, J. S. REED and A. W. NAUMANN, *Bull. Amer. Ceram. Soc.* **55** (1976) 717.
17. T. K. GUPTA, J. H. BECHTOLD, R. C. KUZNICKI, L. H. CADOFF and B. R. ROSSING, *J. Mater. Sci.* **12** (1977) 2421.
18. T. K. GUPTA, *Sci. Sint.* **10** (1978) 205.
19. T. K. GUPTA, F. F. LANGE and J. H. BECHTOLD, *J. Mater. Sci.* **13** (1978) 1464.
20. I. NETTLESHIP and R. STEVENS, *Int. J. High Tech. Ceram.* **3** (1987) 1.
21. F. F. LANGE, *J. Mater. Sci.* **17** (1982) 225.
22. *Idem., ibid.* **17** (1982) 235.
23. *Idem., ibid.* **17** (1982) 240.
24. I. ODA, M. MATSUI and T. SOMA, "Strength and Durability of PSZ Ceramics", paper presented at the International Symposium on Ceramic Components for Engine, Hakone, Japan, October 1983 (Elsevier, London, 1986).
25. M. RUHLE and A. H. HEUER, in "Advances in Ceramics", Vol. 12, "Science and Technology of Zirconia", edited by N. Claussen, M. Ruhle and A. H. Heuer (American Ceramic Society, Columbus, OH, 1984) pp. 14–32.
26. M. RUHLE, N. CLAUSSEN and A. H. HEUER, *ibid.*, pp. 352–70.
27. M. MATSUI, T. SOMA and I. ODA, *ibid.*, pp. 371–81.
28. K. TSUKUMA, Y. KUBOTA and T. TSUKIDATE, *ibid.*, pp. 382–90.
29. H. SCHUBERT, N. CLAUSSEN and M. RUHLE, *ibid.*, pp. 766–73.

30. T. K. GUPTA and C. A. ANDERSON, *Ceram. Engr. Sci. Proc.* **7** (1986) 1150.
31. C. A. ANDERSON and T. K. GUPTA, *ibid.* **7** (1986) 1158.
32. M. MATSUI, T. SOMA and I. ODA, *J. Amer. Ceram. Soc.* **69** (1986) 198.
33. F. F. LANGE, *ibid.* **69** (1986) 240.
34. T. MASAKI, *ibid.* **69** (1986) 638.
35. L. J. SCHIOLER, "Effect of Time and Temperature on Transformation Toughened Zirconias", Technical Report TR 87-29, US Army Materials Technology Laboratory, Watertown, MA, June 1987.
36. J. J. SWAB, "Properties of Yttria–Tetragonal Zirconia Polycrystal (Y-TZP) Materials After Long-Term Exposure to Elevated Temperatures", Technical Report TR 89-21, US Army Materials Technology Laboratory, Watertown, MA, March 1989.
37. J. SUNG and P. S. NICHOLSON, *J. Amer. Ceram. Soc.* **71** (1988) 788.
38. K. NOGUCHI, Y. MATSUDA, M. OISHI, T. MASAKI, S. NAKAYAMA and M. MIZUSHINA, *ibid.* **73** (1990) 2667.
39. K. TSUKUMA and M. SHIMADA, *Amer. Ceram. Soc. Bull.* **64** (1985) 310.
40. A. P. DRUSCHITZ and J. G. SCHROTH, *J. Amer. Ceram. Soc.* **72** (1989) 1591.
41. F. F. LANGE, *ibid.* **66** (1983) 396.
42. F. F. LANGE and M. METCALF, *ibid.* **66** (1983) 398.
43. F. F. LANGE, B. I. DAVIS and I. A. AKSAY, *ibid.* **66** (1983) 407.
44. F. F. LANGE, B. I. DAVIS and E. WRIGHT, *ibid.* **69** (1986) 66.
45. J. WANG and R. STEVENS, *J. Mater. Sci.* **24** (1989) 3421.
46. K. TSUKUMA, K. UEDA and M. SHIMADA, *J. Amer. Ceram. Soc.* **68** (1985) C4–C5.
47. K. TSUKUMA and K. UEDA, *ibid.* **68** (1985) C56–C58.
48. TSK 'Super-Z' (ZrO_2–Al_2O_3 Powder) 3Y20A Grade, Ceramic Series Technical Bulletin 1987–1988 (Toyo Soda Manufacturing Company Ltd, Tokyo, Japan).
49. R. K. GOVILA, "Ceramic Life Prediction Parameters", Technical Report TR 80-18, Army Materials and Mechanics Research Center, Watertown, MA, May 1980.
50. R. K. GOVILA, J. A. HERMAN and N. ARNON, "Stress Rupture Test Rig Design for Evaluating Ceramic Material Specimens", ASME Paper No. 85-GT-181, Gas Turbine Conference, Houston, TX, 18–21 March, 1985.
51. R. K. GOVILA, *J. Amer. Ceram. Soc.* **73** (1990) 1744.
52. *Idem, J. Mater. Sci.* **26** (1991) 1545.
53. D. J. CASSIDY, R. L. VAN ALSTEN and M. E. MILBERG, US Pat. 4866014, 12 September 1989.
54. D. C. HOAGLIN, in "Understanding Robust and Exploratory Data Analysis", edited by D. C. Hoaglin, F. Mosteller and J. W. Tukey (Wiley, New York, 1983) pp. 33–57.
55. J. T. HEALEY and J. J. MECHOLSKY Jr, *Scanning* **4** (1981) 62.
56. *Idem*, "Scanning Electron Microscopy Techniques and Their Application to Failure Analysis of Brittle Materials", ASTM STP 827 (American Society for Testing and Materials, Philadelphia, PA, 1984) pp. 157–81.
57. K. D. REEVE, *Amer. Ceram. Soc. Bull.* **42** (1963) 452.
58. W. H. RHODES, *J. Amer. Ceram. Soc.* **64** (1981) 19.
59. D. E. NIESZ and R. B. BENNETT, in "Ceramic Processing before Firing", edited by G. Y. Onada Jr and L. L. Hench (Wiley Interscience, 1978) pp. 61–73.
60. J. S. REED, T. CARBONE, C. SCOTT and S. LUKASIEWICZ, in "Processing of Crystalline Ceramics", edited by H. Palmour III, R. F. Davis and T. M. Hare (Plenum, New York, 1978) pp. 171–80.
61. R. W. RICE, *ibid.*, pp. 302–22.
62. S. MIZUTA, M. PARISH and H. K. BOWEN, *Ceram. Int.* **10** (1984) 43–48, 83–86.
63. M. V. PARISH, R. R. GARCIA and H. K. BOWEN, *J. Mater. Sci.* **20** (1985) 996.
64. M. L. MECARTNEY, *J. Amer. Ceram. Soc.* **70** (1987) 54.
65. J. DRENNAN and R. H. J. HANNINK, *ibid.* **69** (1986) 541.
66. R. K. GOVILA, *J. Mater. Sci.* **23** (1988) 1141.
67. *Idem, J. Amer. Ceram. Soc.* **65** (1982) 15.
68. F. WAKAI, *Brit. Ceram. Trans. J.* **88** (1989) 205.
69. F. WAKAI, Y. KODAMA and T. NAGANO, *Jpn J. Appl. Phy. Series 2, Lattice Defects in Ceramics* (1989) 57.
70. F. WAKAI, S. SAKAGUCHI and Y. MATSUNNO, *Adv. Ceram. Mater.* **1** (1986) 259.
71. F. WAKAI and H. KATO, *Adv. Ceram. Mater.* **3** (1988) 71.
72. I. W. CHEN and L. A. XUE, *J. Amer. Ceram. Soc.* **73** (1990) 2585.
73. O. D. SHERBY and J. WADSWORTH, *Prog. Mater. Sci.* **33** (1989) 169.
74. T. G. NIEH and J. WADSWORTH, *Acta. Metall. Mater.* **38** (1990) 1121.
75. *Idem, J. Amer. Ceram. Soc.* **72** (1989) 1469.
76. *Idem, J. Mater. Res.* **5** (1990) 2613.
77. *Idem, Ann. Rev. Mater. Sci.* **20** (1990) 117.
78. K. KOBAYASHI, H. KUWAJIMA and T. MASAKI, *Solid State Ionics* **3** (1981) 489.
79. M. WATANABE, S. ITO and I. FUKUURA, in "Advances in Ceramics, Science and Technology of Zirconia II", Vol. 12, edited by N. Claussen, M. Ruhle and A. H. Heuer (American Ceramic Society, Columbus, OH, 1984) pp. 391–8.
80. K. NAKAJIMA, K. KOBAYASHI and Y. MURATA, *ibid.*, pp. 399–407.
81. T. SATO and M. SHIMADA, *J. Amer. Ceram. Soc.* **67** (1984) C212.
82. *Idem, ibid.* **68** (1985) 356.
83. T. SATO, S. OHTAKI and M. SHIMADA, *J. Mater. Sci.* **20** (1985) 1466.
84. K. TSUKAMA and M. SHIMADA, *J. Mater. Sci. Lett.* **4** (1985) 857.
85. M. YOSHIMURA, T. NOMA, K. KAWABATA and S. SOMIYA, *ibid.* **6** (1987) 465.
86. F. F. LANGE, G. L. DUNLOP and B. I. DAVIS, *J. Amer. Ceram. Soc.* **69** (1986) 237.
87. S. Y. CHEN and H. Y. LU, *J. Mater. Sci.* **24** (1989) 453.
88. J. J. SWAB, "Low Temperature Degradation of Y-TZP Materials", Technical Report TR 90-4, US Army Materials Technology Laboratory, Watertown, MA, January 1990.
89. E. H. LUTZ, N. CLAUSSEN and M. V. SWAIN, *J. Amer. Ceram. Soc.* **74** (1991) 11.
90. E. H. LUTZ, M. V. SWAIN and N. CLAUSSEN, *ibid.* **74** (1991) 19.

Received 2 September 1991
and accepted 24 March 1992